

Thomas Majlund Nielsen

# Simulation of Active Matter within a Heterogeneous Topography

Master's thesis in MTFYMA

Supervisor: Paul Gunnar Dommersnes

February 2023



Thomas Majlund Nielsen

# **Simulation of Active Matter within a Heterogeneous Topography**

Master's thesis in MTFYMA  
Supervisor: Paul Gunnar Dommersnes  
February 2023

Norwegian University of Science and Technology  
Faculty of Natural Sciences  
Department of Physics





# Preface

This master thesis marks the end of my master's degree in Applied Physics and Mathematics at NTNU. The foundation for my research was my project thesis "Simulation of Forward and Reverse Ostwald Ripening for Active Matter". That thesis mainly involved replicating results found in previous literature. For my master thesis, I wanted to find a way to apply the knowledge I had attained to research something that had not been done before.

The main remark of my project thesis involved analyzing numerical instabilities emerged in my attempt to simulate matter Model B+ according to numerical details in past literature. When starting with my master project, my first endeavour was to try to resolve said numerical instabilities, before focusing on the main topic of my master thesis, which was implementing a heterogeneous topography. I had expected this to take several months. Luckily, I was able to make contact with one of the creators of Active Model B+, Professor Elsen Tjhung, who provided me with source code that allowed me to create a stable simulation.

While my goal had been to simulate Active Model B+, programming it in a heterogeneous topography proved a challenge equal to making a stable simulation. Doing so involved numerical challenges that, to my knowledge after extensive research, had not been solved in literature. At least not in a manner which was useful to my simulation. For this reason, I changed focus to simulating the simpler Active Model B, which had not been applied to a heterogeneous topography. Doing so, I found interesting and surprising dynamics involving Active Model B. I decided thus to focus my research on documenting these new dynamics.

I would like to extend my thanks to Professor Elsen Tjhung for the source code he provided. While I ultimately ended up not using any of it, it helped in that I managed to create a stable Active Model B+ simulation early on, saving me weeks, if not months of work that I would end up not using anyways.

I would also like to Professor Paul Dommersnes for his proposal of topics, as well as his guidance throughout this project.

# Abstract

This thesis pertains to the simulation of active matter within a heterogeneous topography. Active matter theories have often been used to model the behavior of living matter, particularly microorganisms. While several models exist, few have endeavored to model the behavior of active matter within heterogeneous topography, which is the topography of most biological systems. Experiments involving the motion of microorganisms in heterogeneous topography indicate that the topography dramatically alters the dynamics of such active matter. Changes include altering the motion, position, size of microorganism collectives and sometimes even arresting their development.

As we had previously worked on Active Matter phase separation Models B and B+ for our project thesis, we sought to implement these models in a heterogeneous topography of solid particles. Our motive was to observe the interaction between active matter and solids in such a topography and to see how our findings compared with results found in literature. While we had desired to simulate both models, AMB+ proved exceedingly difficult to simulate with a heterogeneous topography. As such, we instead focused our efforts on AMB.

We simulated AMB using a second-order central finite difference scheme. We created a heterogeneous topography by inserting blocks of solid matter into the computational domain, restricting the area in which the active matter could reside. We modeled the interaction on the boundary layer between the active and solid matter using immersed Neumann Boundary conditions.

Our model displayed several of the properties found in relevant literature. We observed the topography altering the size, position, and motion of active matter clusters in AMB and, at times, arresting their development. Beyond that, based on the activity level, the topography fundamentally altered the dynamics of AMB. Clusters of active matter were continuously destroyed and repaired in a dynamic reminiscent of the reversed Ostwald ripening modeled by AMB+. The dynamics were also highly chaotic and noise-sensitive, making the trajectory of the active matter clusters difficult to predict.

We attribute these new dynamics to conflict to how the active matter minimizes its free energy, which is achieved by reducing the phase-separation interface. Adhering to solid matter gives the active matter another way to remove parts of the interface, making this behavior preferable. Active clusters thus arrest near solid particles, preventing macroscopic aggregation. The systems attain a steady state of mesoscopic Ostwald ripening as they minimize local free energy at the cost of being unable to minimize global free energy.

Systems with strong activity arrive at a steady state consisting of cycles of lowering free energy, followed by free energy increases as clusters tear apart and reform. Because of this circular dynamic, we predict the system may never reach a stable state. This dynamic is, however, dependent on the relationship between the total area of the clusters, and that covered by the particles.

# Sammendrag

Denne Masteroppgave omhandler simulering av aktiv materie innen heterogen topografi. Aktiv materie teorier blir ofte brukt til å modellere bevegelsen til levende materie, særdeles mikroorganismer. Flere modeller for aktiv materie eksisterer, men få har modellert oppførselen til aktiv materie innen heterogen topografi, som er topografien de fleste mikroorganismer befinner seg i. Eksperimenter angående mikroorganismer antyder topografien de befinner seg i endrer dynamikken deres substansielt. Dette inngår ting som endring av bevegelse, størrelse, posisjon til mikroorganismenes aggregater, og noen ganger fullstendig arrest av dem.

Motivert av vårt tidligere arbeid med Aktiv Materie fase-separasjons modellene B og B+, ville vi implementere disse modellene i en heterogen topografi av solide partikler. Vi ønsket å oppdage samhandlinger mellom aktiv og solid materie, samt sammenlikne funnene våre med det funnet i relevant litteratur. Vi ønsket å simulere både Aktiv Modell B og B+, men fant ut at å modellere AMB+ i en heterogen topografi involverte store utfordringer. Derfor fokuserte vi heller på AMB.

Vi simulerte AMB med en andre order sentral differanse metode. Vi lagde en heterogen topografi ved å sette solid objekter i simuleringsrommet, som begrenset områdene den aktive materien kunne befinne seg. Vi modellerte samhandlingen mellom den aktive og solide materien ved bruk av oppslukte Neumann grensebetingelser.

Modellen vår viste fram flere av egenskapene funnet i relevant litteratur. Vi observerte at topografien endret størrelsen, posisjonen, og bevegelsen til aktiv materie klyngene i AMB, samt til tider arresterte dem. Videre, basert på aktivitetsnivået til materien kunne topografien fullstendig endre dynamikken til AMB. Aktiv materie klynger ble kontinuerlig ødelagt og reparert i en dynamikk ganske lik den modellert av AMB+. Dynamikken var også kaotisk og støy-sensitiv. Dette medførte at bevegelsesmønstrene til den aktive materien ble vanskelig å forutse.

Vi tillegger denne nye dynamikken til konflikt i hvordan den aktive materien minimere sin frie energi, som den gjør ved å redusere grensesnittet mellom fasene. Ved å legge seg på solid materie, forsvinner store deler av grensesnittet, som gjør denne oppførselen foretrukket for systemet. Dette arresterer klyngene, som forhindrer makroskopisk aggregering. Systemet ender i en tilstand av mesoskopisk Ostwald modning, der de minimerer lokal fri energi ved kostnad av den globale frie energien. Systemer med sterk aktivitet ender i en tilstand av sykluser mellom synking av den frie energien, fulgt av økning der klyngene blir revet i stykker før de så gjendanner seg. Grunnet denne dynamikken, forutser vi at systemet aldri når en stabil tilstand. Denne dynamikken der derimot avhengig av forholdet mellom arealet til klyngene og arealet dekket av de solide partiklene.

# Contents

|          |  |           |
|----------|--|-----------|
| <b>1</b> | <b>Introduction</b>  | <b>1</b>  |
| <b>2</b> | <b>Theory</b>  | <b>3</b>  |
| 2.1      | Phase Separation Models for Active Matter . . . . .  | 3         |
| 2.2      | The Cahn-Hilliard Model . . . . .  | 4         |
| 2.3      | Active Model B . . . . .   | 6         |
| 2.4      | Active Model B+ . . . . .  | 8         |
| 2.5      | Heterogeneous topography . . . . .   | 9         |
| <b>3</b> | <b>Computational Implementation</b>  | <b>12</b> |
| 3.1      | Simulating Active Model B . . . . .  | 12        |
| 3.2      | Simulating Active Model B+ . . . . .   | 14        |
| 3.3      | Implementing a heterogeneous topography . . . . .  | 15        |
| 3.4      | The AMB+ boundary condition problem . . . . .  | 20        |
| <b>4</b> | <b>Procedure and Results</b>   | <b>22</b> |
| 4.1      | Procedure . . . . .  | 22        |
| 4.2      | Simulations with no noise . . . . .  | 24        |
| 4.3      | Simulation of a passive system with noise . . . . .  | 27        |
| 4.4      | Simulation with weak activity and noise . . . . .  | 29        |
| 4.5      | Simulation with strong activity and noise . . . . .  | 32        |
| 4.6      | Simulation with initial stable state and activity . . . . .  | 35        |
| 4.7      | Simulation with negative activity . . . . .  | 38        |
| 4.8      | Additional experiment: Simulation with<br>partially-homogeneous and partially-heterogeneous<br>topography. . . . . | 40        |

|          |  |           |
|----------|--|-----------|
| 4.9      | General results . . . . .  | 41        |
| <b>5</b> | <b>Discussion</b>  | <b>42</b> |
| 5.1      | Interaction between active and solid matter . . . . .                | 42        |
| 5.2      | The effect of Heterogeneous topography on Ostwald ripening . . . . . | 43        |
| 5.3      | Dynamics with noise . . . . .  | 43        |
| 5.4      | The effect of $\lambda$ . . . . .                                    | 45        |
| 5.5      | Interpretation of the newfound dynamics . . . . .                    | 46        |
| 5.6      | Future development . . . . .   | 47        |
| <b>6</b> | <b>Conclusion</b>  | <b>49</b> |

# Chapter 1

## Introduction

Within physics, living beings display unique dynamics that one cannot find amongst non-living matter. Organisms are capable of independent, self-induced movement, which is not easily analyzed by physical laws. An apt example is humans, who can move even if nothing external spurs them. In turn, human movements are too complex and spurious that one can, for now, make a physical model predicting their motion.

However, living creatures can form collectives that have collective motion. Examples of this are bird flocks, fish schools, and bacterial clusters. When joining such a flock, organisms tend to lose their independence, instead adopting the general movement of the collective. This generalization of previously independent has allowed for the creation of physical models for the motion of living creatures. Such living collectives are modeled as active matter, matter capable of self-induced motion[1]. For this thesis, we intend to simulate such a model.

In our case, we focus on microorganisms. So far, several different active matter models have been proposed to explain the motion of microorganisms. Often these take place in a homogeneous topography [2]. A topography is the arrangement of physical features in a space. A homogeneous topography is a topography with the same physical features everywhere. An intuitive example would be a flat plane, which is also the topography in previous simulations of the model we are working with. Conversely, there has been scant development to study what effect a heterogeneous topography has on the dynamics of active matter[2].

By heterogeneous topography, we mean that the space where the matter resides is not homogeneous and contains obstacles that can alter the movement of the objects. An intuitive example would be a city with numerous buildings that prevent certain movement paths. Studying the potential effects topography has on microorganisms is important, as virtually all microorganisms live in heterogeneous topographies, mainly the bodies of larger organisms. Thus, we wanted to simulate how microorganisms, a form of active matter, might behave in such a space.

Our research was motivated by the report "The environment topography alters the way to multicellularity in *Myxococcus xanthus*" [2] by Ramos et al., which explored how heterogeneous topography affects the nucleation of the bacteria "Myxococcus xanthus". The heterogeneous topography in the report above involved placing silica particles in the space containing the M.Xanthus. These silica particles acted like obstacles to the bacteria, preventing bacteria from residing in specific areas. The topography had a significant effect on the collective motion of the bacteria, altering their aggregation. Thus we endeavored to simulate

an active model in a heterogeneous topography to discover if it affected active systems.

For our simulation, we deploy Active Model B[3] and Active Model B+[4]. The model active matter using active phase separation fluid mechanics. We previously worked on these models in our project report, and thus we decided to use them again, but this time with a heterogeneous topography. Of interest was seeing if we would observe the behavior discovered by Ramos et al.. The concepts of these models are detailed in "Scalar  $\phi^4$  field theory for active-particle phase separation"[3] by Wittowski et al. and "Cluster Phases and Bubbly Phase Separation in Active Fluids: Reversal of the Ostwald Process" by Cates et al. [4]. Henceforth we shall refer to these models as AMB and AMB+.

AMB and AMB+ are relatively recent models for active matter. We found no literature about how these models would behave with a heterogeneous topography. As such, we looked to literature about similar models for passive fluids to create our own. In addition to simulating the fluid representative of active organic matter, we introduce solid particles into the system. These force the active matter to change its course upon contact, altering the system's dynamics and potentially the whole aggregation process.

In this report, we go into the theory of active model B and B+, how we simulate them numerically with appropriate boundary conditions and go into the specific details of programming the simulation before analyzing the findings as well as see how they match up with the results in Ramos et al. [2].

# Chapter 2

## Theory

### 2.1 Phase Separation Models for Active Matter

Active matter is matter in which constituents can move, even bereft of an external force or potential acting on them. They achieve this through self-propulsion through isothermal consumption of energy[5] from their surroundings. Generally, active matter categorizes living beings, as they tend to have personal mobility mechanisms. Active matter models have been used to analyze the movement of collectives of living creatures, with bacterial collectives being of key interest to this thesis[2].

Bacteria are capable of self-propulsion, fuelled by consuming nutrients in the surrounding water, meaning we can model them as active matter. We specifically sought to model microorganisms as an active fluid, which is a soft matter fluid which components can self-propel. For this reason, active fluids can behave similarly to clusters of bacteria. If suspended in still water, the bacteria will propel themselves around through motility, consuming various microorganisms for energy[6]. The dynamics of active fluid particles are a form of Brownian motion, with the overall motion of the collectives being dependent on the collective Brownian motion of the constituents[7].

A particular property of active fluids is that time-reversal symmetry is locally broken, allowing for a phenomenon known as motility-induced phase separation[4]. Motility is the ability of an organism to move independently through metabolism. Self-propelled particles tend to accumulate where they move slowly, which occurs when said particles are in high density. This process causes a positive feedback loop, resulting in such particles aggregating [8]. This results in the formation of areas with a high density of active matter and a low density of active matter.

This process is similar to fluid phase-separation, which is a phenomenon where a fluid separates into two immiscible phases[8]. An illustrative example of phase separation, though not involving active matter, is that of a vinegar-oil emulsion. One may combine oil and vinegar into a single fluid, but they will eventually separate back into oil and vinegar phases due to their chemical properties.

Phase-separation dynamics are commonly evaluated using the Cahn-Hilliard equation, or Passive Model B, on which AMB and AMB+ are based. In our case, the active fluid has a binodal density, with a dense liquid phase and a dilute vaporous phase[4]. The process is

similar to spinodal decomposition, in which a thermodynamic state spontaneously separates into two phases[4]. In comparison to the biological system, one can imagine the system describes the density of bacteria.

The dynamics of such a system are largely driven by Ostwald ripening[4]. Ostwald ripening is a physical process where droplets of a fluid or fluid phase immersed in another immiscible fluid or fluid phase move to minimize their surface area[9]. Continuing the oil/vinegar analogy, an example of this process is droplets of oil on top of the vinegar surface gathering into a single large droplet over time. This behavior can occur in phase-separated active fluids, where the dense and dilute phases gather into a single large droplet respectively[4].

## 2.2 The Cahn-Hilliard Model

To explain the functions of AMB and AMB+, we start with the Cahn-Hilliard equation for phase separation. The Cahn-Hilliard equation is based on the free energy functional

$$F = \int dx^n \left[ \frac{a}{2}\rho^2 + \frac{b}{4}\rho^4 + K(\nabla\rho)^2 \right] \quad (2.1)$$

Here,  $\rho$  is the density of the fluid. The first two terms constitute the Helmholtz free energy of the system. Assuming  $a < 0$  and  $b > 0$ , the function  $a\rho^2 + b\rho^4$  has two minima at  $\rho = \pm\sqrt{a/b}$ . These represent binodal densities, two coexisting densities at the free energy minima. This equation thus models a fluid with minimal free energy if it separates into two phases, each with one of the binodal densities.

From this we functional we derive the chemical potential of the phase-separating fluid as a function of the density  $\rho$

$$\mu_{eq} = \frac{\delta F}{\delta\rho} = a\rho + b\rho^3 - K\nabla^2\rho \quad (2.2)$$

The first two terms constitute the bulk chemical potential  $f(\rho)$ , instilling the binodal in the system, resulting in phase separation if there are any gradients in the system. Between the two phases emerges an interface with a mean value between the two binodal densities. Said interface is defined by the  $K|\nabla\rho|^2$  term. This term causes the gradient between the two phases to diffuse, allowing a continuous transition from one phase to another. That is, ensuring the density does not suddenly jump at the transition point. Notably, the fluid is still most stable when in one of the two phases. Thus, while this interface is necessary, the system will tend to minimize its presence.

The  $K$  term thus defines the free energy cost of changes in  $\phi$ [4] and punishes gradients. As  $\phi$  generally only changes at the phase-separation interface, the effect of the  $K$  term is that the surface area of droplets will be restricted. This, in turn, drives the Ostwald ripening of the system. The global free energy is minimal when the total surface area (or surface length in two dimensions) is minimal, which is most easily accomplished by aggregating the droplets of each phase into a single body. The Mechanics of the Cahn-Hilliard equation are illustrated in Fig.2.1.

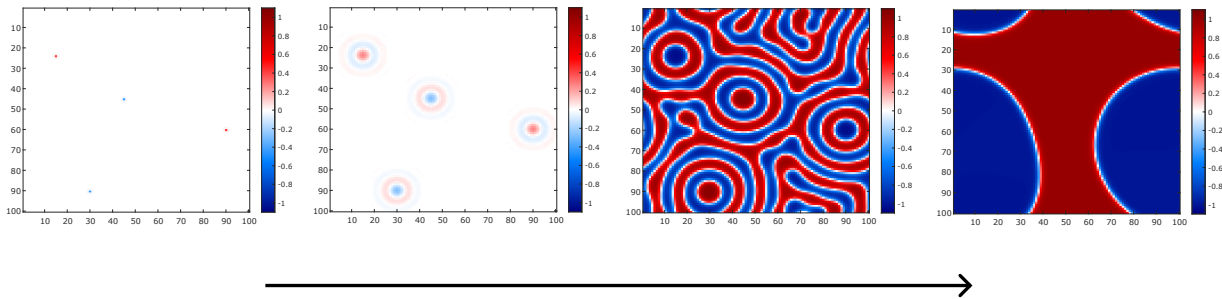


Figure 2.1: Illustration of the Cahn-Hilliard phase separation dynamic. An initially homogeneous fluid is perturbed, as seen in the first picture. This perturbation causes the fluid to begin dividing into two phases, as seen in the second picture. One dense, marked by the red color, and one dilute, marked by the blue color. Eventually, the fluid across the entire lattice divides into two phases, with a white diffused interface between them. These phases then undergo Ostwald ripening, resulting in the final picture. The two phases have each joined into one large body, as this is the geometry that minimizes the diffused interface. We note that we used periodic boundaries, meaning any fluid element exiting at a boundary will enter the system again on the opposite boundary. We made this illustration using our simulation, the details of which will be specified in Chapter. 3.

There are two manners in which Ostwald ripening occurs. One involves two or more droplets of the same phase making contact and joining. The second manner involves small droplets dissipating into the surrounding, opposite phase. Here, droplets are destroyed, with their mass dispersing throughout the system before being deposited in larger droplets. In the end, the system reaches a steady state with a single, large body of each phase[4].

The time evolution of  $\rho$  can then be derived as

$$\frac{\partial \rho}{\partial t} = M(\rho) \Delta \mu_{eq} \quad (2.3)$$

Where  $M(\rho)$  is a mobility function, defining how easily a fluid element can move as a function of its density.

We wanted to simplify the equation and thus transformed the density  $\rho$  to  $\phi = \frac{2\rho - \rho_H - \rho_L}{\rho_H - \rho_L}$ , where  $\rho_H$  and  $\rho_L$  are the densities of the dense and dilute phases respectively. This transform changes our binodal densities to  $\rho_H \rightarrow \phi_H = 1$  and  $\rho_L \rightarrow \phi_L = -1$ . The interface attains the middle value between  $\phi_H$  and  $\phi_L$ . Using the above transformation, this density corresponds to  $\phi = 0$ [4]. This transform simplifies our equation and allows us to express the chemical potential of a phase-separating fluid as

$$\mu_{eq} = \frac{\delta F}{\delta \phi} = a\phi + b\phi^3 - K\nabla^2 \phi \quad (2.4)$$

From this, we derive the current vector as

$$\mathbf{J} = -M(\phi) \nabla \mu_{eq} \quad (2.5)$$

And we express the evolution of  $\phi$  as the divergence of the current

$$\partial_t \phi = -\nabla \cdot (\mathbf{J} + \sqrt{2DM}\Lambda) \quad (2.6)$$

Or writing it out

$$\partial_t \phi = M(\phi)\Delta(a\phi + b\phi^3 - K\nabla^2\phi) + \sqrt{2DM}\nabla \cdot \Lambda \quad (2.7)$$

$\Lambda$  is a random noise variable with Gaussian distribution around a zero mean with unit variance [4]. This thermal noise is affected by the fluid temperature magnitude  $D$ . Together  $\Lambda$ ,  $D$ , and  $M$  express the noise in the system as a function of temperature.

We note that all quantities involved are denoted in natural units, including the system's time[4]. What the values correspond to in a natural system is still an area of study. For the sake of simplicity, we set  $M(\phi) = 1$  and let  $D$  range from 0 to 1. We also set  $a = -1$  and  $b = 1$ , meaning our binodal in the passive case would be  $\phi_1 = 1$  and  $\phi_2 = -1$ .

The addition of the noise allows for the total free energy of the system to increase occasionally. These increases do not violate the thermodynamics of the system, as the noise term adds randomly distributed kinetic energy to the system. As a result, gradients will randomly appear, which in turn causes the free energy to increase. In turn, the  $K$  term will work to flatten these gradients.

Henceforth, the simple Cahn-Hilliard equation, or "Passive Model B", will be referred to as PMB.

## 2.3 Active Model B

AMB models active matter as an active fluid. That is a fluid consisting of soft matter capable of self-propulsion. We thus imagine microorganisms as a soft matter fluid, comprising one of the phases emerging from the Cahn-Hilliard dynamic. This model was formulated in "Scalar  $\phi^4$  field theory for active-particle phase separation" by Wittoski et.al[3].

AMB advances the Cahn-Hilliard equation to model active matter's phase separation. This is accomplished by adding a non-integrable term that breaks time-reversal symmetry. Namely  $\lambda(\nabla\phi)^2$ , where  $\lambda$  is a term determining the degree of activity. This term is the simplest non-integrable second-degree term that one can add to the chemical potential[10]. We then express an active chemical potential  $\mu_{act}$  as

$$\mu_{act} = \frac{\delta F}{\delta \phi} = a\phi + b\phi^3 - K\nabla^2\phi + \lambda(\nabla\phi)^2 \quad (2.8)$$

Which gives us the current

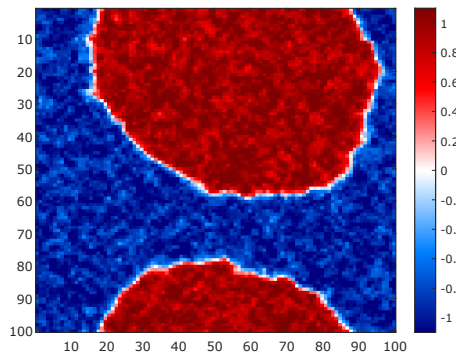
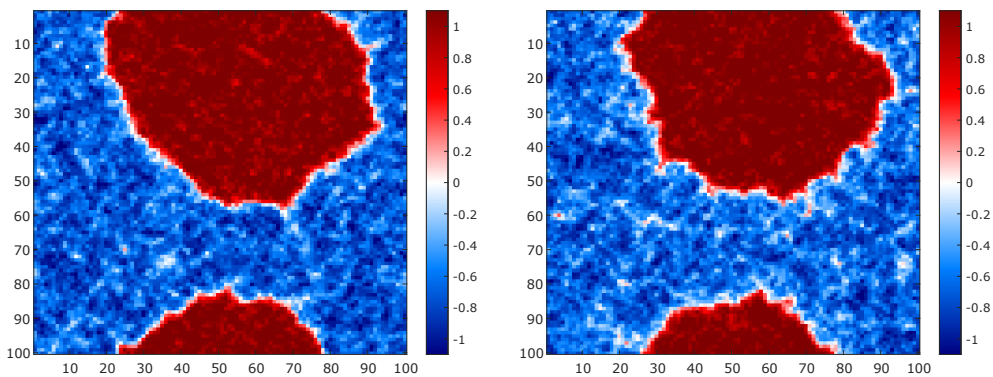
$$\mathbf{J} = -\nabla\left[\frac{\delta F}{\delta \phi} + \lambda|\nabla\phi|^2\right] \quad (2.9)$$

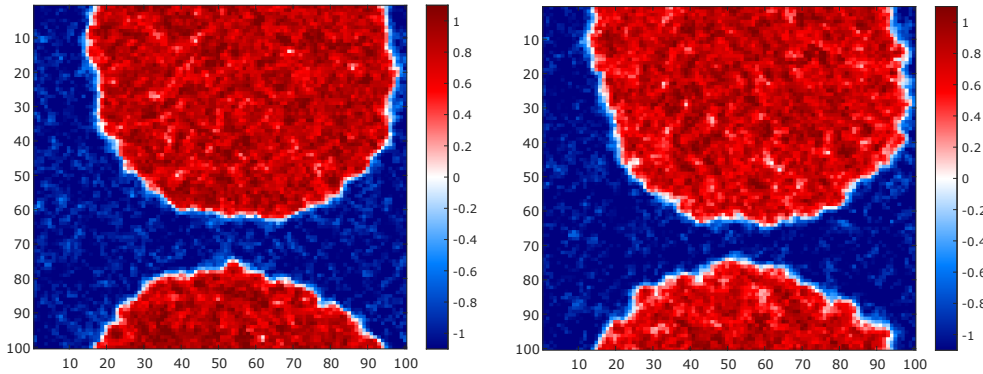
Adding the noise term, we arrive at the time evolution of  $\phi$

$$\partial_t \phi = \nabla^2(a\phi + b\phi^3 - K\nabla^2\phi + \lambda|\nabla\phi|^2) + \sqrt{2DM}\nabla \cdot \Lambda \quad (2.10)$$

The  $\lambda$  term models quorum-sensing. In the biological sciences, quorum-sensing is the ability of bacteria to detect and respond to the nearby cell population. In AMB, this means active fluid elements can detect nearby gradients. Comparatively, In PMB, the Ostwald ripening dynamic is driven by the pressure difference across the phase-separation interface, which pushes the phase-separated clusters around until they reach a state of pressure equilibrium. With the quorum-sensing term, the individual fluid elements can detect the local gradient to determine if they are close to the interface or near areas with the same density[4]. This extra information makes them actively seek ways to minimize their free energy, thus making the matter "active".

The effect of this active term is that the system's binodal changes from the passive case. The two phase  $\phi_1$  and  $\phi_2$ , allowing for densities that exceed  $|\phi| = 1$ . This facet emerges due to the active matter attempting to minimize the phase-separation interface by condensing further or dispersing the fluid[3]. A positive  $\lambda$  value will make the system denser. The dense phase will shrink in area, while the dilute phase will grow. Both of their average  $\phi$  values will increase. A negative  $\lambda$  will have the inverse effect. The strength of these effects grows with  $|\lambda|$ , as shown in Figs. 2.2, 2.3 and 2.4 below. We note that these illustrations were made using our simulation tool, which will be expanded upon in Chapter 3.

Figure 2.2:  $\lambda = 0$ Figure 2.3:  $\lambda = 1$  and  $\lambda = 2$

Figure 2.4:  $\lambda = -1$  and  $\lambda = -2$ 

We note that, depending on the system's geometry, the free energy can increase from the passive case. The positive  $\lambda$  decreases the free energy in the above case. This is because we have modeled a dense droplet surrounded by the dilute phase. Conversely, the energy is increased for negative  $\lambda$  as the droplet increases in size while the surroundings disappear.

For a biological interpretation of these reactions, one can imagine the dense phase as a cluster of bacteria. Positive  $\lambda$  results in a quorum sensing that informs the bacteria to gather closely. Conversely, negative  $\lambda$  informs the bacteria to avoid other bacteria.

## 2.4 Active Model B+

AMB+ advances AMB by adding another time-reversal symmetry-breaking term to the current, namely  $\zeta\Delta\phi\nabla\phi$ . This term models short-range interaction between active matter particles[4]. This model was formulated in "Cluster Phases and Bubbly Phase Separation in Active Fluids: Reversal of the Ostwald Process" by Cates et al. With this model, the time derivative of  $\phi$  is expressed as

$$\partial_t\phi = \nabla^2(a\phi + b\phi^3 - K\nabla^2\phi + \lambda|\nabla\phi|^2) + \nabla \cdot (\zeta\Delta\phi\nabla\phi) + \sqrt{2DM}\nabla \cdot \Lambda \quad (2.11)$$

AMB+ models "reverse Ostwald ripening" in active fluids, limiting the maximally allowed radius of droplets. Any droplets that exceed this radius will begin to divide. This leads the system to a steady state involving numerous droplets of finite size. The reverse Ostwald ripening dynamic of AMB+ is illustrated in Fig. 2.5 below.

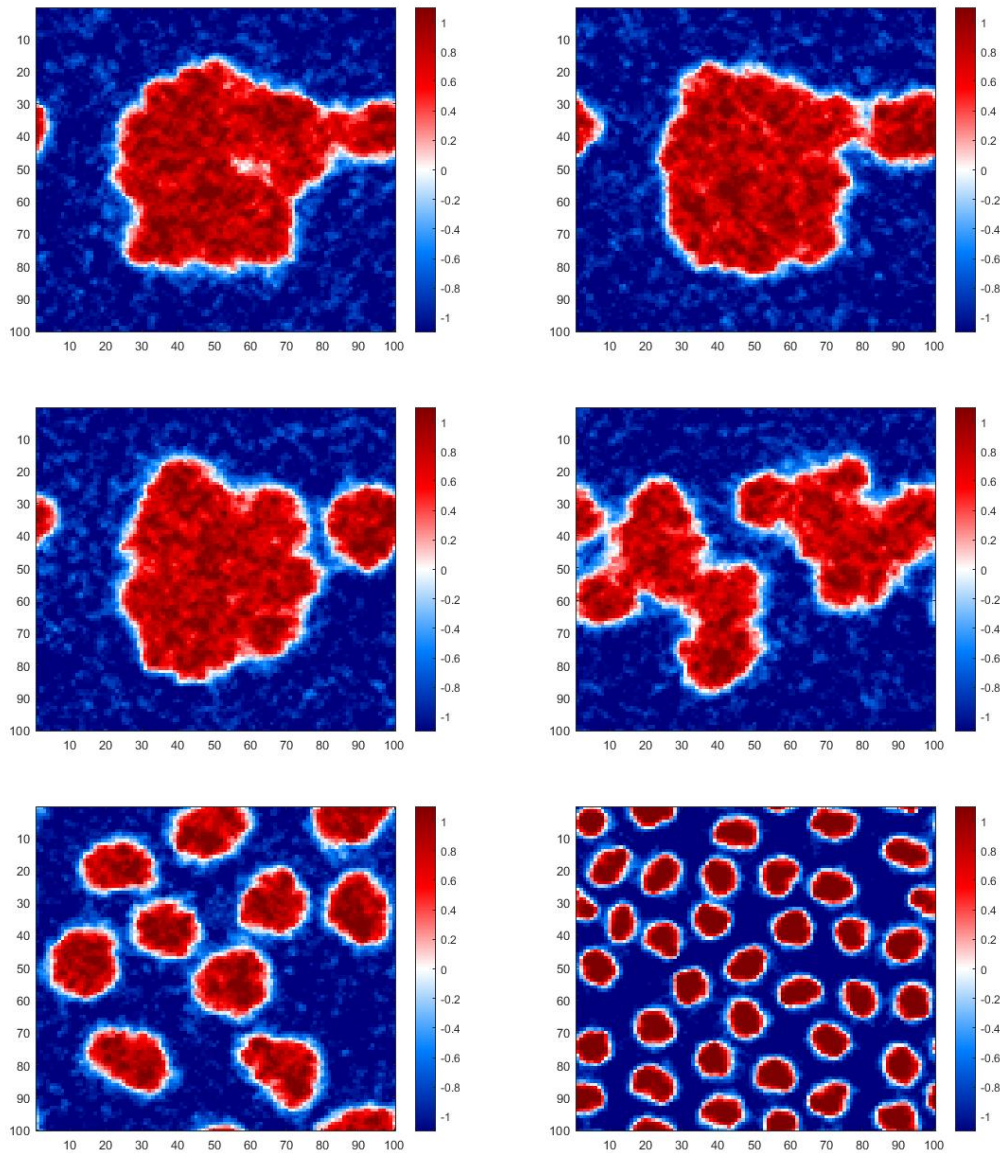


Figure 2.5: Active fluid modeled by AMB+. The dense droplet undergoes reverse Ostwald ripening as its size exceeds what the fluid’s chemical properties allow. As such, the droplet begins tearing and dividing into smaller droplets. This illustration was made using our simulation, details of which we will denote in Chapter. 3.

We will not go into great detail regarding AMB+ for reasons that we will detail in Section 3.5.

## 2.5 Heterogeneous topography

In the paper that motivated our research [2], we observed that the topography where active matter resides affects the system’s dynamics. The researchers analyzed a colony of the bacteria *Myxococcus Xanthus* and how they respond to a heterogeneous topography. In a homogeneous topography, *M. Xanthus* enter a ” multicellularity ” phase, where the cells aggregate to form collectives known as ”fruiting bodies”. They do this by creating slime trails for other bacteria to follow, which gather them into large clusters[2].

The researchers altered the topography by randomly adding silica particles to the dish containing the bacteria. These particles considerably altered the dynamics of the fruiting bodies, altering their size, shape, number and in some cases arresting their development. A significant reason for this was the cells’ tendency to adhere to the silica particles, disrupting the

usual aggregation of the cells. As a result, fruiting bodies ended up being smaller than they would be in a homogeneous topography. An important observation noted in the paper is that the particles did not merely hinder aggregation by acting as obstacles to said aggregation but affected the very manner in which the bacteria aggregated[2].

The tendency to aggregate is similar to Ostwald ripening. AMB is a model of active matter which dynamics are primarily driven by Ostwald ripening. Similarly, AMB+ models Ostwald ripening up to a limited size[4]. For this reason, we propose that these models can be used to model multicellularity. As these models have primarily involved homogeneous topography, we created our own active models within heterogeneous topography. We did this by adding blocks representing solid particles into the simulation space. These blocks would be immovable and would not permit the active fluid to penetrate them. Compared to the paper by Ramos et al.[2], one can view the dense phase of the fluid as aggregates of bacteria and the solid particles as silica particles.

To simulate solid matter, we defined areas in the computational space to exist outside the computational domain of the fluid. These areas would be our solid matter, and we would have to ensure there was no mass exchange between these areas and the fluid.

We would have to define appropriate boundary conditions for the boundary between the fluid and solid surfaces. We defined the areas the fluid was allowed to exist as  $\Omega_{in}$  and the solid objects as  $\Omega_{out}$ . We denoted the interface between the two domains as  $\partial\Omega$ .

Two boundary conditions were needed as AMB and AMB+ are fourth-order partial differential equations. For appropriate boundary conditions, we looked to literature pertaining to the Cahn-Hilliard Neumann problem, detailing how the Cahn-Hilliard equation should behave with Neumann boundary conditions[11]. The natural choice would be, according to literature [11], the two Neumann boundary conditions

$$J_n|_{\partial\Omega} = \partial_n\mu_{eq}|_{\partial\Omega} = 0 \quad (2.12)$$

$$\partial_n\phi|_{\partial\Omega} = 0 \quad (2.13)$$

Where  $J_n$  is the current normal to the solid surface, and  $\partial_n$  denotes the derivative along the normal to the boundary surface.

The first boundary condition signifies that there cannot be a current normal to a solid surface. There can be no flux in or out of the solid particle. This condition allowed us to simulate a solid surface and ensured the conservation of mass in the system.

The second boundary condition states that there is no  $\phi$  gradient along the normal direction to a solid surface. This boundary condition is natural, considering the system should evolve in such a manner as to minimize the free energy of the system. This condition accomplishes this by eliminating the normal component of  $\nabla\phi$  in  $K|\nabla\phi|^2$ [12][13].

The physical interpretation of the second boundary condition is that the diffused interface separating the two phases intersects the solid surface at a static  $\frac{\pi}{2}$  angle[11]. This is because the interface is defined by the density gradient between the two phases. Thus, the interface will always be normal to the gradient of  $\phi$ . Eliminating the normal component to this means

the interface will only have a parallel gradient near a solid surface, forcing the interface to intersect the wall normally.

Physically speaking, such an interface should only emerge between the separate phase bodies. There is, in general, no reason why such an interface should emerge between the fluid and a solid surface, i.e., that the density suddenly increases/decreases towards the opposite phase near a solid surface. By applying this boundary condition, we ensure this does not happen.

This boundary condition also allows us to model the behavior found in the paper by Ramos et al., where bacteria adhered to solid surfaces[2]. Due to the Cahn-Hilliard equation's tendency to minimize the phase-separation interface, droplets would also adhere to solid surfaces, as doing so will eliminate part of the interface. As such, with this boundary condition, the active matter will also tend to adhere to the solid object we insert into the topography, allowing us to simulate this behavior.

The thermodynamics of the system demands the bulk free energy is strictly non-increasing. This was established in the paper "A review on the Cahn-Hilliard equation: classical results and recent advances in dynamic boundary conditions" by Hao Wu[11]. The equation is as follows

$$\begin{aligned}
 \frac{d}{dt} E_{bulk}(\phi) &= \int_{\Omega} d^2r [K \nabla \phi \cdot \nabla \partial_t \phi + F'(\phi) \partial_t \phi] \\
 &= \int_{\Omega} d^2r [\mu \partial_t \phi] = \int_{\Omega} d^2r [\mu \nabla \cdot (M \nabla \mu)] \\
 &= - \int_{\Omega} d^2r [\nabla \mu \cdot (M \nabla \mu)] + \int_{\partial \Omega} d^2r [\mu (M \nabla \mu \cdot \mathbf{n})] \\
 &= - \int_{\Omega} d^2r [M |\nabla \mu|^2]
 \end{aligned} \tag{2.14}$$

The integral along  $\partial \Omega$  in the third line disappears due to our no flux condition. We can thus be sure the bulk free energy is non-increasing with our boundary conditions.

We note that the boundary conditions are informed by literature pertaining to the Cahn-Hilliard Neumann boundary problem, which describes a passive fluid. We cannot neglect the possibility that special considerations might exist for our active  $\lambda$  term. As AMB and AMB+ are relatively new models, scarce literature has been produced evaluating what effect interaction with solid matter could have on such an active fluid.

We note, however, that AMB dynamics are similar to passive phase-separation [4]. The only real difference is that the binodal is altered. The Ostwald ripening dynamic remains. As a result, AMB will attempt to minimize the phase-separation interface. When contacting a solid surface, the interface will be minimal if it intersects the surface at a  $\pi/2$  angle. As such, according to the dynamics of AMB, this boundary condition is appropriate.

AMB+ has a different dynamic, as it also involves reverse Ostwald ripening. Notably, however, AMB+ causes reverse Ostwald ripening by limiting the area of droplets, not necessarily by demanding an increase of the global interface. Droplets smaller than the maximal area will still undergo Ostwald ripening to reduce the free energy down to what the maximal size of droplets allows. As such, this boundary condition should be acceptable for AMB+ as well.

# Chapter 3

## Computational Implementation

### 3.1 Simulating Active Model B

We solved the AMB equation numerically using the finite difference method. To represent the fluid, we created a two-dimensional lattice containing the values of  $\phi$  discretized along the x- and y-directions as  $\Delta x$  and  $\Delta y$ . We enumerated these values with the integer variables  $i$  and  $j$  in the x- and y-directions, respectively. As such, the discrete spatial coordinates were denoted as  $(i\Delta x, j\Delta y)$  with the corresponding  $\phi$  value  $\phi_{i,j}$ . The discretization is illustrated below in 3.1.

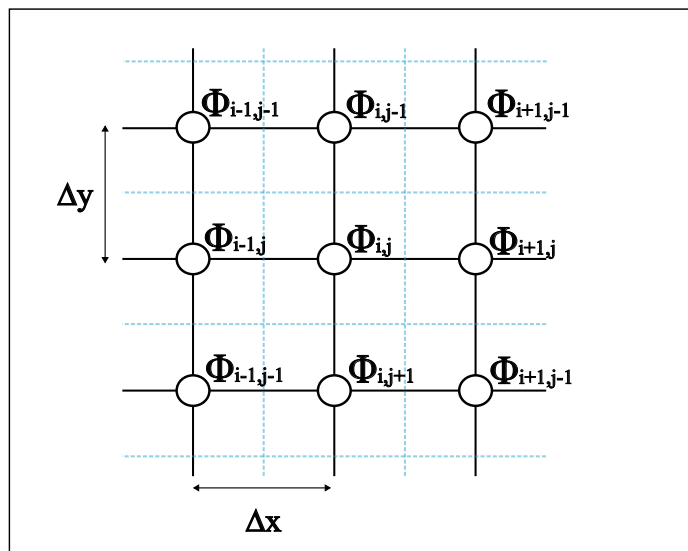


Figure 3.1: Illustration of how the system was discretized. The white nodes represent the discrete points of  $\phi$  used in the calculation. The dotted blue lines are the areas where the discrete values  $\phi_{i,j}$  are contained.

During our previous work on simulating AMB and AMB+, we used the "Euler-Maruyama" method to evaluate the time-evolution of  $\phi$ . This method is a version of the explicit Euler method used to approximate stochastic processes numerically. This is because the noise can be viewed as a Wiener process, which is a continuous-time, stochastic process with variance  $\sqrt{\delta t}$ [14]. We decided to employ this method once more for our system with Neumann boundary conditions.

We discretized time as  $\Delta t$  and denote the discrete values of the time-evolution as  $\phi_{i,j}^n$ . The AMB equation can, as found in the paper by Cates et al[4], then be expressed as

$$\frac{\phi_{i,j}^{n+1} - \phi_{i,j}^n}{\Delta t} = -\nabla \cdot (\mathbf{J}_{i,j}^n - \sqrt{2MD}\nabla \cdot \mathbf{\Gamma}_{i,j}^n) \quad (3.1)$$

$\mathbf{\Gamma}_{i,j}$  is a Gaussian random variable with zero mean and unit variance. The  $\mathbf{\Gamma}$  variable, along with its coefficient, provided the noise of the system[4].

Using the previous equation, we can express the successive steps of the time-evolution of  $\phi$  as

$$\phi_{i,j}^{n+1} = \phi_{i,j}^n - \Delta t \nabla \cdot \mathbf{J}_{i,j}^n - \sqrt{\frac{2MD\Delta t}{\Delta x \Delta y}} \nabla \cdot \mathbf{\Gamma}_{i,j}^n \quad (3.2)$$

The simulation was computed across a square lattice of dimension  $L \times L$ , where  $L$  was 100. We used a finite difference scheme to calculate system development, and the lattice was thus discretized in the x- and y-direction, with  $\Delta x = \Delta y = 1$ . We decided upon a  $\Delta t = 0.01$ .

We used central finite difference at each point to calculate the derivatives. While our previous simulation of AMB+ required high-order differentials, we found one can achieve a stable simulation of Active Model B with the second-order space-centered differential operators

$$\partial_x \phi_{i,j} = \frac{\phi_{i+1,j} - \phi_{i-1,j}}{2\Delta x} \quad (3.3)$$

$$\partial_y \phi_{i,j} = \frac{\phi_{i,j+1} - \phi_{i,j-1}}{2\Delta y} \quad (3.4)$$

$$\partial_x^2 \phi_{i,j} = \frac{\phi_{i-1,j} + \phi_{i+1,j} - 2\phi_{i,j}}{\Delta x^2} \quad (3.5)$$

$$\partial_y^2 \phi_{i,j} = \frac{\phi_{i,j-1} + \phi_{i,j+1} - 2\phi_{i,j}}{\Delta y^2} \quad (3.6)$$

In our project report, we calculated second derivatives by using the first derivatives twice. Effectively, we calculated  $\mathbf{J}$  first and then calculated this vector's divergence. However, using this scheme, coupled noise proved highly unstable, leading to unrealistic phase separation. As such, we chose the method of first calculating  $\mu_{act}$  using the equations for the second derivative above and then finding the time-evolution of  $\phi$  using the second derivative of  $\mu_{act}$ .

We chose this method because the differentiation method mentioned above strongly relates the derivative at a point with every other point next to it rather than its adjacent points. We end up with a strong correlation between alternating points comparatively small correlation between neighboring points. Effectively, going along a line on the simulation surface, we get a system oscillating between two slightly different solutions, creating unrealistic grid patterns.

This discretization was used to calculate all terms of the form  $\nabla f$  and  $\nabla \cdot f$ . Divergence terms were calculated simply by summing the x- and y-version of Eq. 7 acting on the quantity being evaluated like this

$$\nabla \cdot f = \frac{f_{i+1,j} - f_{i-1,j}}{2\Delta x} + \frac{f_{i,j+1} - f_{i,j-1}}{2\Delta y} \quad (3.7)$$

To deal with the boundaries around the computational domain we used periodic boundary conditions.

$$\partial_x \phi_{i_{max},j} = \frac{\phi_{i_{max}-1,j} - \phi_{1,j}}{2\Delta x} \quad (3.8)$$

$$\partial_x \phi_{1,j} = \frac{\phi_{2,j} - \phi_{i_{max},j}}{2\Delta x} \quad (3.9)$$

$$\partial_x^2 \phi_{1,j} = \frac{\phi_{i_{max},j} + \phi_{2,j} - 2\phi_{1,j}}{\Delta x^2} \quad (3.10)$$

$$\partial_x^2 \phi_{i_{max},j} = \frac{\phi_{i_{max}-1,j} + \phi_{1,j} - 2\phi_{i_{max},j}}{\Delta x^2} \quad (3.11)$$

With a similar scheme for derivatives in the y-direction. This was done to conserve mass, as any matter that crossed a boundary would re-enter the system at the opposite boundary.

## 3.2 Simulating Active Model B+

Simulating AMB+ required more specialized tools. In both AMB and AMB+, the system nucleates droplets. However, by nature, AMB+ limits the size of said droplets. If the droplets are of sufficiently small size, the system quickly becomes numerically unstable[15][16]. This instability emerges because we get large gradients from small concentrated droplets, while the diffused interface does not have the time to emerge. The gradient, coupled with the  $\phi^3$  term, causes the system to grow unstable. Thus AMB+ requires high-order differential operators. Firstly, AMB+, as computed in previous literature, used several different definitions for the  $\nabla$ - and  $\Delta$ -operators[15].

For the passive, integrable terms, the first derivative is discretized as

$$\partial_x^2 \phi_{i,j} = \frac{-\frac{1}{560}\phi_{i-4,j} + \frac{8}{315}\phi_{i-3,j} - \frac{1}{5}\phi_{i-2,j} + \frac{8}{5}\phi_{i-1,j} - \frac{205}{72}\phi_{i,j} + \frac{8}{5}\phi_{i+1,j} - \frac{1}{5}\phi_{i+2,j} + \frac{8}{315}\phi_{i+3,j} - \frac{1}{560}\phi_{i+4,j}}{\Delta x} \quad (3.12)$$

With a similar operator for indices of  $j$ . In our simulation, we used these operators on the term  $\mu_{eq} = a\phi + b\phi^3 - K\Delta\phi$  to calculate a "passive current"  $\vec{J}_p$

$$\vec{J}_p = \nabla \mu_{eq} \quad (3.13)$$

Eq. 3.12 was then applied again to calculate  $\nabla^2\mu_{eq}$ . Similarly, this operator was used to calculate the noise-divergence term.

To model the effect of the active terms in a stable manner, all direct derivatives of  $\phi$ , including  $K\Delta\phi$ , were calculated using differential operators that also model contributions along the axis normal to the direction of the operator. The first derivatives for  $\phi$  was then calculated as

$$\partial_x\phi = \frac{0.1(\phi_{i+1,j+1} + \phi_{i+1,j-1} - \phi_{i-1,j+1} - \phi_{i-1,j-1}) + 0.3(\phi_{i+1,j} - \phi_{i-1,j})}{\Delta x} \quad (3.14)$$

$$\partial_y\phi = \frac{0.1(\phi_{i+1,j+1} + \phi_{i-1,j+1} - \phi_{i+1,j-1} - \phi_{i-1,j-1}) + 0.3(\phi_{i,j+1} - \phi_{i,j-1})}{\Delta y} \quad (3.15)$$

While  $\Delta\phi$  was calculated as

$$\begin{aligned} \nabla^2\phi = & \frac{-0.5(\phi_{i+1,j+1} + \phi_{i-1,j+1} + \phi_{i+1,j-1} + \phi_{i-1,j-1})}{\Delta y\Delta x} \\ & \frac{+2(\phi_{i,j+1} + \phi_{i,j-1}) + \phi_{i+1,j} + \phi_{i-1,j} - 6\phi_{i,j}}{\Delta y\Delta x} \end{aligned} \quad (3.16)$$

We then used then Eq. 3.16 to calculate  $K\Delta\phi$  and the active terms, comprising an "active current"  $\vec{J}_a$ .

$$\vec{J}_a = -\nabla((\lambda\phi)^2) + \zeta\Delta\phi\nabla\phi \quad (3.17)$$

We then used Eq. 3.14 and Eq. 3.14 on the active current to calculate the divergence of  $\vec{J}_a$ , which was then added to the divergence of the passive current and the noise to calculate the time-evolution of  $\phi$ [15].

### 3.3 Implementing a heterogeneous topography

To facilitate the simulation of a complex domain, we used a method similar to the one used in "A conservative numerical method for the Cahn–Hilliard equation with Dirichlet boundary conditions in complex domains" by Li et al.[17]. Here, the researchers constructed a conservative numerical solution of the Cahn-Hilliard equation, constricted by arbitrarily shaped solid walls on which  $\phi$  has Dirichlet boundary values. We adopt their numerical methods but insert the solid walls into the fluid domain and use Neumann boundary conditions instead.

We defined two areas in the computational domain,  $\Omega_{in}$  and  $\Omega_{out}$ .  $\Omega_{in}$  defined areas the fluid was allowed to exists and  $\Omega_{out}$  being solid matter were the fluid could not reside. We denoted the boundary between the domains  $\partial\Omega$ , which is the surface where our Neumann Boundary conditions would come into effect. We imagined the domain composition as illustrated in 3.2.

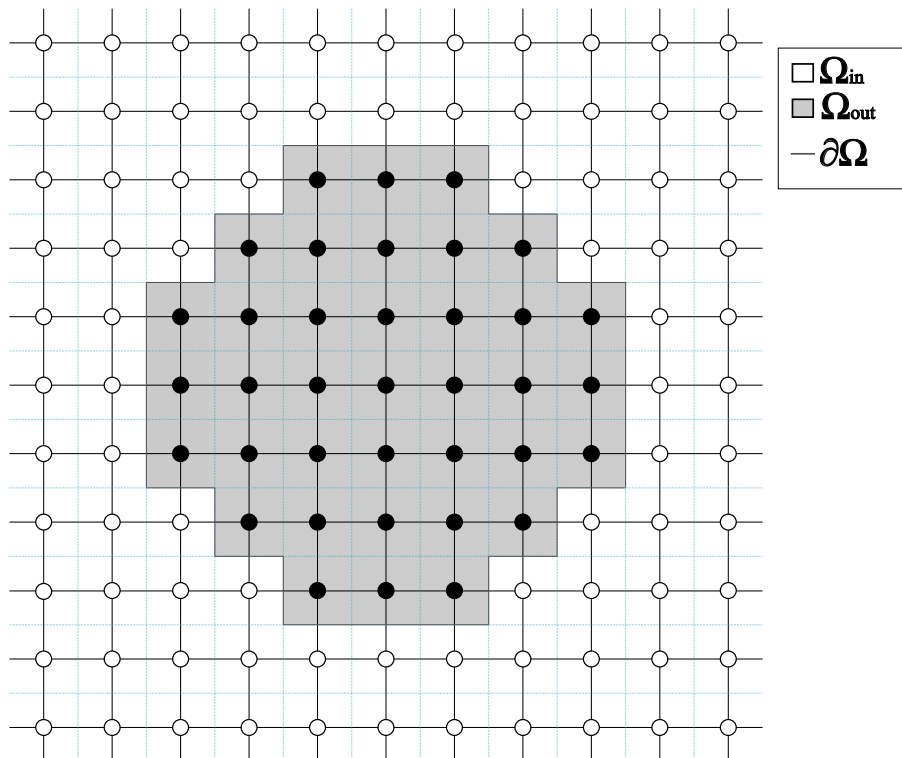


Figure 3.2: Illustration of how the system was discretized with solid matter particles. The white nodes in  $\Omega_{in}$  represent the discrete points of  $\phi$  used in the calculation. The grey area  $\Omega_{out}$  is the solid matter. The black nodes are the discrete computational points where  $\phi$  would have otherwise been. The boundary between the two domains is  $\partial\Omega$

To separate the two domains in computation, we defined a function  $G(x, y)$ , where

$$G(x, y) = \begin{cases} 1 & x, y \in \Omega_{in} \\ 0 & x, y \in \Omega_{out} \end{cases} \quad (3.18)$$

By multiplying  $\phi$  with  $G$ , we eliminated any computation in  $\Omega_{out}$ . The shape of  $\Omega_{out}$ , and thus  $G$ , was defined arbitrarily.

To implement our Neumann boundary conditions, we used the ghost point method, meaning that for any calculation requiring a computational point inside a solid particle, we inserted computational "ghost points" in that position. This ghost point would have a virtual value that made the discrete calculation fulfill the boundary conditions. The way we imagined the boundary conditions is illustrated in Fig. 3.3.

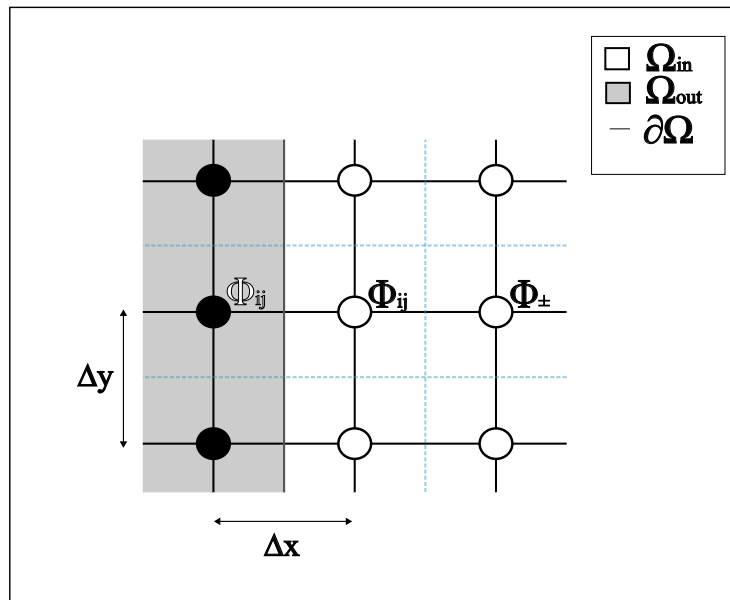


Figure 3.3: The black nodes are the ghost points inside  $\Omega_{out}$ .  $\phi$  does not actually exist here, but by giving this virtual  $\phi$  value the same value as the first point outside the solid surface, the boundary condition  $\partial_n \phi_{i,j}|_{\partial\Omega} = 0$  is fulfilled.

From Fig. 3.3: As  $\partial_n \phi_{i,j}|_{\partial\Omega} = 0$ , this means that the ghost point inside the solid object should have the same value as its neighboring  $\phi_{i,j}|_{\partial\Omega}$  along the surface-normal. Applying central finite difference to the middle point on the boundary gives us  $(\phi_{i,j} - \phi_{i,j})/\Delta x$ , which is equal to zero. The boundary condition is thus indeed fulfilled. Equivalently, we can also fulfill the  $\partial \mu_{ni,j}|_{\partial\Omega} = 0$  boundary condition using the same method for values of  $\mu$ .

These boundary conditions enter our calculations when we calculate  $\partial_t \phi$  near the surface of a solid object. Defining the point neighboring  $\phi_{i,j}$  near the surface as  $\phi_{\pm}$  depending on its orientation to the surface, we get the following equation for the second derivative

$$\partial_n^2 \phi_{i,j}|_{\partial\Omega} = \frac{\phi_{\pm} - \phi_{i,j}}{\Delta x^2} \quad (3.19)$$

To implement the no-flux boundary condition, we used a similar method. As  $\nabla_n \cdot J|_{\partial\Omega} = \partial_n \mu_{eq}|_{\partial\Omega} = 0$ , we similarly get that

$$\partial_n^2 \mu_{i,j}|_{\partial\Omega} = \frac{\mu_{\pm} - \mu_{i,j}}{\Delta x^2} \quad (3.20)$$

We also needed a way for the program to evaluate the orientation of the boundaries. We created a matrix  $C(x, y)$  with the same dimensions as  $\phi(x, y)$ . It has the property that it

$$C(x, y) = \begin{cases} 2 & x, y \in \Omega_{in} \\ 1 & x, y \in \partial\Omega \\ 0 & x, y \in \Omega_{out} \end{cases} \quad (3.21)$$

The boundary condition  $\partial_n \phi_{i,j}|_{\partial\Omega} = 0$  could then easily be implemented by simply finding a point where  $C(x, y) = 1$ , finding the adjacent  $C(x, y) = 2$  and then use that information to decide the surface normal.

For  $C(x, y) = 0$ , the simulation would deal with a fluid far from solid matter. If this were the case, the simulation would compute the system's evolution as usual. If  $C(x, y) = 1$ , the system was at a boundary point, and would be computed with the specified Neumann boundary conditions. Any point with  $C(x, y) = 1$  would be next to a point with  $C(x, y) = 2$ , which would let the simulation find the orientation of the fluid element in relation to the solid objects. This was necessary as to allow the simulation to decide what direction the normal derivative took.

We then decided on what manner of objects we would place into the system. In general, we used "pseudo-circles", objects that approximate a circular shape, as seen in Fig 3.2. We did this as we imagined the solid blocks as large cells or objects similar to the silica particles in the multicellularity paper, and we thus wanted to approximate a "round" shape.

An issue with the "pseudo-circles" is that the interaction they have with the fluid is not isotropic. As seen in Fig 3.2, the "sides" of the object parallel to the x- and y-axis are flat, while the other sides are shaped more like stairs. For an actual circle, none of these shapes exist. This implementation has no physical meaning and emerges as a result of the numerical approximation we made.

To resolve this, we attempted to implement immersed Neumann boundary conditions. This means evaluating the system equation using boundary points not restricted by the numerical grid. In essence, we wanted objects with boundaries shaped like the circle in Fig. 3.4

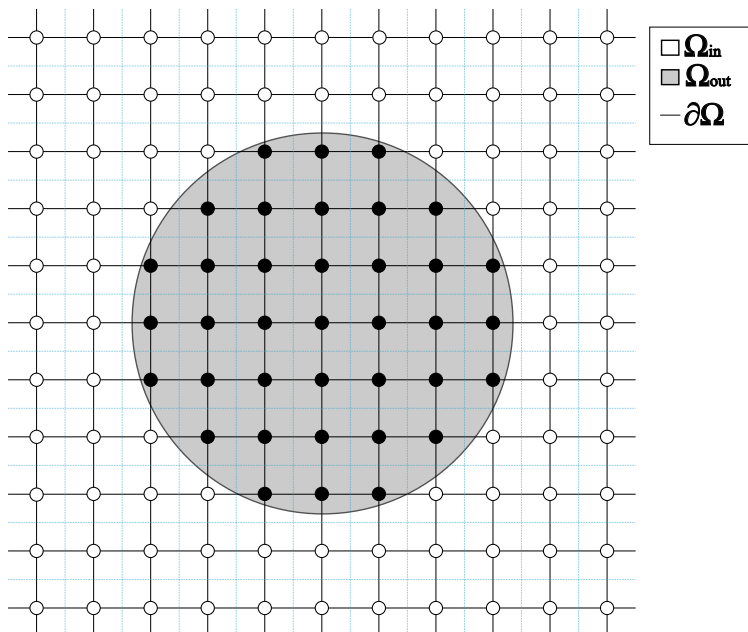


Figure 3.4: The solid particle now has a circular shape.

While the fluid equation itself would still be evaluated on the numerical grid, the boundaries were not. As shown above, we would make the fluid behave as if there were an actual round boundary in the grid. To do this, we employed a method used in the book "Numerical Solution of Partial Differential Equations: An Introduction" by K. W. Morton and D. F. Mayers[18]. In this book, the second spatial derivative of a conserved quantity  $U$  is calculated using an inhomogenous grid spacing. To simplify, we use the generalized coordinate  $z$ . Near the boundary, the computation will look like the one illustrated in Fig. 3.5

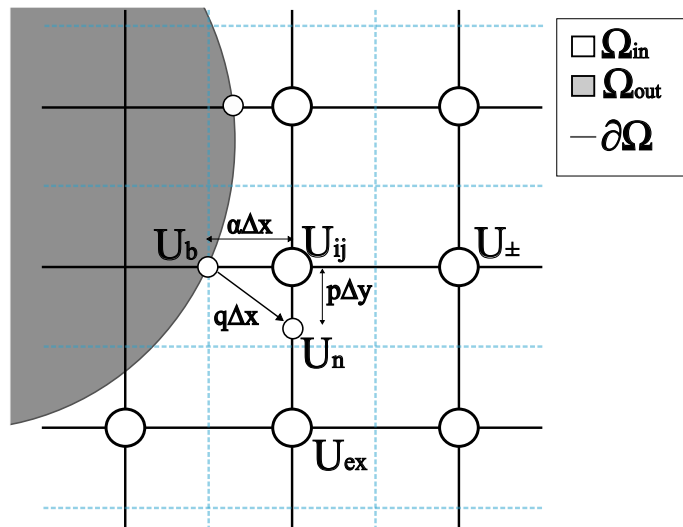


Figure 3.5: The black nodes are the ghost points inside  $\Omega_{out}$ .

If the distance between the point nearest boundary and the nearest computational point  $U_{i,j}$  is  $\alpha\Delta z$ , where  $\alpha$  is smaller than the average grid spacing, then the second derivative along the can be expressed as[18]

$$\partial_z^2 U = \frac{2}{(\Delta z)^2} \left[ \frac{U_B}{\alpha(\alpha+1)} - \frac{U_{i,j}}{\alpha} + \frac{U_{\pm}}{\alpha+1} \right] \quad (3.22)$$

Here,  $U_B$  is the value of  $U$  at the immersed boundary,  $U_{i,j}$  is the point on the computational grid closest to the boundary, and  $U_{\pm}$  is the computational point on the other side on  $U_{i,j}$  away from  $U_B$ , along the relevant axis.

This equation allowed us to compute second derivatives at the computational nodes nearest the solid boundaries. The book does not, however, explicitly denote an operator for the first derivative, and literature denoting it proved difficult to find. We can, however, make an appropriate second-order central finite difference operator consistent with the operator above.

We take advantage of the fact that the ordinary central difference operator is the numerical average of the forward and backward finite difference operators. Denoting them as  $\partial_{z+}U$  and  $\partial_{z-}U$  respectively, we can express the central finite difference operator as

$$\frac{\partial_{z+}U + \partial_{z-}U}{2} = \frac{1}{2} \left( \frac{U_+ - U}{\Delta z} + \frac{U - U_-}{\Delta z} \right) = \frac{U_+ - U_-}{2\Delta z} = \partial_z U \quad (3.23)$$

Using the same equation near the immersed boundary gives us two equations for the first derivative, both depending on the orientation of the boundary on the orientation of the grid points to the boundary.

$$\partial_z U = \frac{1}{2} \left( \frac{U_B - U}{\alpha\Delta z} + \frac{U - U_-}{\Delta z} \right) = \frac{U_B + (\alpha-1)U - \alpha U_-}{2\alpha\Delta z} \quad (3.24)$$

$$\partial_z U = \frac{1}{2} \left( \frac{U_+ - U}{\Delta z} + \frac{U - U_B}{\alpha\Delta z} \right) = \frac{\alpha U_+ + (1-\alpha)U - U_B}{2\alpha\Delta z} \quad (3.25)$$

With this, we had all the operators needed to calculate immersed Neumann boundary conditions for AMB. To make these calculations, however, we needed to find the quantity  $U_B$ , the value of  $U$  at the immersed boundary. Within our model, two quantities fit this role. Namely the values of  $\phi$  and  $\mu$  at the surface boundary. As luck would have it, we have two fitting boundary conditions for these values. For both cases, we have that

$$\partial_n U_B = 0 \quad (3.26)$$

To solve this numerically, we defined a value  $U_n$ , which would be the first point where the normal from  $U_B$  intersects with the numerical grid, as shown in the Fig 3.5. Assuming the distance between these points is  $q\Delta z$ , we approximate the above equation as[18]

$$\partial_n U_B = \frac{U_B - U_n}{q\Delta z} = 0 \quad (3.27)$$

Which means

$$U_B = U_n \quad (3.28)$$

We would then find  $U_n$  by linear interpolation between its two neighbors on the grid[18]. As shown in Fig 3.5, the distance between  $U_n$  and  $U_{i,j}$  is  $p\Delta y$ , and the distance to  $U_n$  other closest neighbouring point  $U_{ex}$  is  $(1-p)\Delta y$ , where  $p < 1$ . As we have set that  $\Delta x = \Delta t = 1$   $U_n$  can be found by linear interpolation between  $U_{ex}$  and  $U_{i,j}$  as

$$U_n \approx pU_{ex} + (1-p)U_{i,j} \quad (3.29)$$

Inserting this into Eq. 3.22, we arrive a boundary condition for boundaries not restricted by the numerical grid.

### 3.4 The AMB+ boundary condition problem

We experienced several challenges in attempting to model the boundary conditions for AMB+. These challenges were related to the high-order differential operators needed to create a stable simulation. We had initially wanted to simulate both AMB and AMB+ using the operators defined for AMB+. That way, we would have a single model and could study the effect of the parameters involved. We, however, soon found that attempting to implement the necessary Neumann boundary conditions involved a numerical challenge, and solutions eluded us in our literature search.

Neumann boundary conditions are reasonably easy to implement for the second-order central difference operator, as they only model the interaction between the solid surface and the fluid element a single discrete spatial point away. For example, suppose the point(s) at  $(i+1, j)$  resides within a solid particle. In that case, any special interaction with the solid object will only affect the point(s) evolution of  $\phi_{i,j}$ . But with higher order differential operators, we create interaction between the solid particles and the fluid further away from it.

For example, using the eight-point stencil used in the BPS paper, a point  $\phi_{i,j}$  left of the solid surface requires four points inside the solid object for calculation. Meanwhile,  $\phi_{i-1,j}$  requires three such points. We could implement the Neumann boundary conditions for  $\phi_{i,j}$  by setting all the ghost point  $\phi_{i+1,j} = \phi_{i,j}$ , which would fulfill the boundary condition as mentioned previously. We do not know, however, know what the other ghost point, deeper into the solid particle, should have for the calculation of  $\phi_{i,j}$ . We have not yet determined what effect these conditions should have on points further from the solid particle but still within the computational domain of the particle.

Using the previous example,  $(i-1, j)$  will depend on  $(i+1, j)$ ,  $(i+2, j)$  and  $(i+3, j)$ . We are, however, uncertain what effects the ghost points inside the solid particle should have on this point. We could not find literature that analyzed this problem for a normal fluid, let alone an active one. We attempted to implement them in the simplest manner possible: to have the four ghost points inside the solid object mirror their four counterparts in the fluid domain.

The effect of this interaction was a sort of "leakage", between the solid objects and the fluid outside, causing the mass to leak out from or into the solid particles. In time, one of the phases would start growing at the other's expense, making the system unrealistic. We thus abandoned this endeavor and focused on creating a model using the second-order central differential operators. This scheme could easily be made conservative compared to the eight-point stencil above.

We attempted to model AMB+ using the second-order central difference operator instead of the eight-point stencil while keeping the other operators. This did allow us to implement conservative Neumann boundary conditions, but only for infinitely long surfaces. When the solid objects we created had finitely long surfaces, or in other words, corners, the system would again experience a leakage. This is because of the interaction between corner points and the combined  $x, y$  operators. As the corner points are connected to surfaces in both the  $x$  and  $y$ - directions, special considerations must be taken for the boundary conditions here. We could not find literature providing a solution to this problem.

As such, with all the difficulties encountered, we decided to set AMB+ aside indefinitely and instead focused on our AMB simulations.

# Chapter 4

## Procedure and Results

### 4.1 Procedure

We created a heterogeneous topography by arbitrarily placing circles representing solid matter onto the computation lattice. We decided to focus our analysis on a singular topography which we dubbed  $\Omega_{main}$ . The solid particles were assigned a radius  $r_0 = 5.35$ . Solid objects would need to have some  $\phi$  value standing in for them for plotting purposes. We chose the value  $\phi = 0$  in areas where solid particles resided. This choice was made, in part, because it was easy to implement with our  $G(x, y)$  function. Secondly, it served as a safety mechanism for calculating the bulk free energy. If we accidentally forgot to exclude the solid areas from our measurements, the bulk free energy in these areas would become zero. Our  $\Omega_{main}$  topography is illustrated in Fig.4.1.

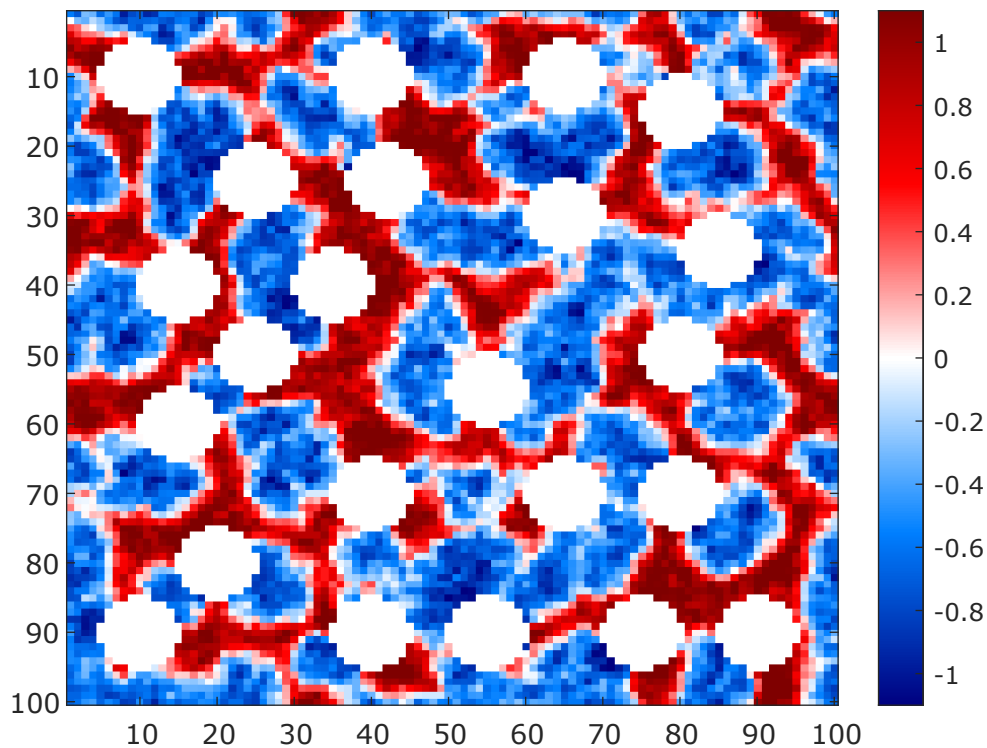


Figure 4.1: System with initial density  $\phi_0 = -0.3$  and  $\lambda = 1$ . The free energy is plotted next to it on a logarithmic scale. The system reached its steady state around  $t = 30000$ .

While our circles appear blocky in the illustration, composed of squares assembled in a circular shape, our immersed boundary conditions give them the properties of real round objects in computations. This discrepancy emerges as a limitation in the plotting tool. We considered making the particles appear more circular by increasing their size. However, keeping the particles spaced out would require a larger lattice, requiring more computational time. As such, we kept it as is.

As we were working with a phase-separation model for active matter, we had to analyze two separate regimes, namely the two phases. As we were mainly interested in the topography's effect on aggregation, we decided to focus on one phase. We chose the dense phase as representative of active matter and the dilute phase as areas where the active matter was scarce. As the system's dynamics are symmetric, this choice does not matter much but felt natural, as we imagined high-density to be the best representation of clusters containing matter. Thus, unless otherwise specified, when we refer to active matter, we refer to the dense phase, which is color-coded as red. The dilute phase can be viewed as fluid with very little active matter and is color-coded as blue.

We would initiate systems with a uniform density  $\phi_0$ . This value would usually be negative  $-1 < \phi_0 < -0.2$ . We did this to ensure the dense phase filled up the smallest area. This reduced the chance that the periodic boundaries would connect the dense phase at multiple ends, which could interfere with the dynamics.

Variable parameters were the initial density  $\phi_0$ ,  $\lambda$ , and the temperature  $D$ , the last of which determined the strength of the noise. The paper by Cates et.al[4], which inspired our research, allowed  $D$  to vary between 0 and 1.  $D = 0$  corresponded to no noise. In our initial experiments,  $D = 0.5$  and above caused such noise as to make it exceedingly difficult for droplets to form at all. Generally, we decided on a noise level corresponding to  $D = 0.1$ , as this did not interfere much with the system's dynamics and gave a reasonable time until the systems would reach their steady state.

Preliminary tests showed us that  $\lambda \in [-2, 2]$  resulted in noteworthy dynamics. As such, we focused our simulations on systems with  $\lambda$  in this range.

We would create a plot of the system for every 100th unit of our dimensionless time. We arrived at this period after trying out several. 100 time units gave the system time to evolve notably, but not abruptly, giving us time to analyze individual plots while also providing us with continuous oversight of the development of the system. We would take snapshots of the system when it did something qualitatively noteworthy. By this, we mean dynamics not displayed in a homogeneous topography.

We also plotted the free energy along with the system's time evolution. In general, the system would undergo massive changes in the early stages of nucleation while the free energy was relatively high. During the first few thousand time units, the free energy would drop exponentially due to the initial phase separation and the large number of droplets. After this, the free energy would drop at a slower, near-linear rate. As a result, the nucleation process also slowed down. Early simulation indicated that systems generally needed tens of thousands of time units to reach a steady state.

Because of how the free energy developed over long periods, we decided to plot the free energy as a function of time on a logarithmic scale. Using a linear time scale created a dense

and uninformative plot. Using a logarithmic time scale allowed us to compare the large initial drop in free energy to the relatively minor changes as the system neared its steady state.

We calculated the free energy by summing all discrete terms comprising the free energy.

$$\sum_{i,j} -\frac{\phi_{i,j}^2}{2} + \frac{\phi_{i,j}^4}{4} + K|\nabla\phi_{i,j}|^2$$

Because of the time scale, we also usually put a computational time limit of  $t = 100000$ . Such computations took the better part of a day to simulate, and systems would usually reach a steady state by then.

As the system's dynamics are driven by decreasing free energy and Ostwald ripening, we used two phenomena to decide when the system appeared to reach a steady state.

First was the aggregation. If all the active matter had gathered into a single droplet through Ostwald ripening or had otherwise ceased evolving with time in any noticeable way, we considered that the system had reached a final, steady state and that further simulation would not yield an interesting result.

Secondly, we determined the free energy had reached a minimum when it reached a near-constant minimal value or oscillated around such a value. Notably, due to the noise, which constantly created gradients, there would always be some motion in the system, and it would not be possible for it to truly reach a minimum. But, if the energy seemed to oscillate around a certain energy level, and the shapes of the droplets were not changing notably, we felt it safe to say the system had reached a steady state. To determine if the energy had reached a minimum, we checked if it had not changed considerably for 20000 time units, as this was generally ample time for any change to occur.

We discovered some surprising dynamics involving AMB within the heterogeneous topography during our proceeding. For this reason, we made numerous simulations not initially planned to uncover and learn more about AMB and how it acts within its topography. Notably, it displayed properties similar to that of AMB+. For this reason, we made the choice to focus our efforts exclusively on AMB.

## 4.2 Simulations with no noise

First, we would simulate systems absent of noise. This was done so we could observe the effect the solid particles had on a deterministic system. We initiated systems with initial density  $\phi_0 = -0.3$ , and perturbed them as to instigate phase-separation. For comparison, we also simulated systems with the same total mass, but without the solid particles. The free energy was calculated along with the systems.

First we wanted to simulate a passive fluid, i.e one with  $\lambda = 0$ . This was to find out how a phase-separated fluid would behave in a heterogeneous topography, as we had found no literature detailing this.

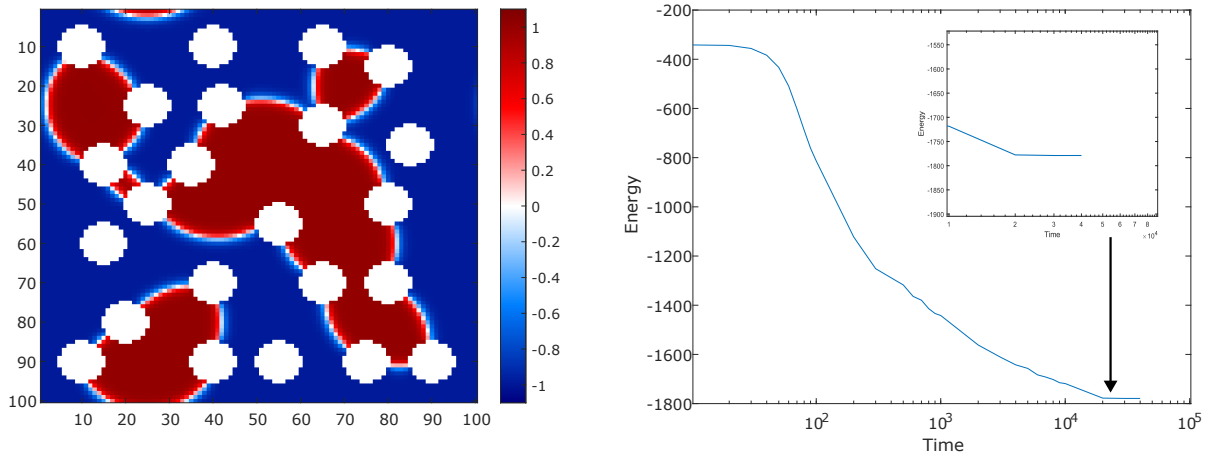


Figure 4.2: System with initial density  $\phi_0 = -0.3$  and  $\lambda = 0$ . The free energy is plotted next to it on a logarithmic time scale. The system reached its steady state around  $t = 20000$ .

The system underwent Ostwald ripening, but the clusters took shape according to our solid particle topography. The steady state consists of numerous different clusters, rather than a single one, like would happen in a homogeneous topography, as plotted below.

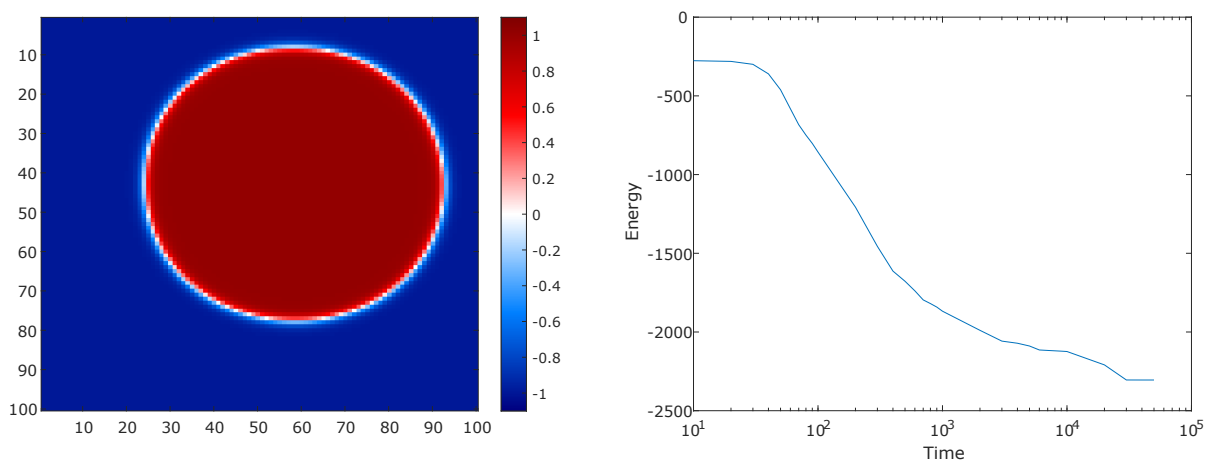


Figure 4.3: System with the same mass and parameters as in Fig 4.2, without solid particles. The free energy is plotted next to it on a logarithmic time scale. The system reached its steady state around  $t = 30000$ .

We would then add activity by setting  $\lambda = \pm 1$  resulting in the following steady states.

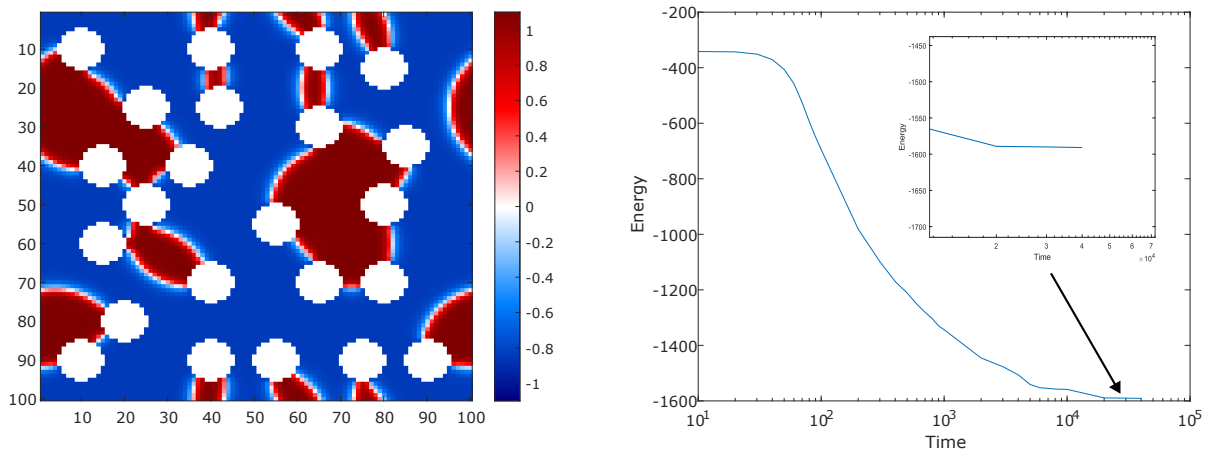


Figure 4.4: System with initial density  $\phi_0 = -0.3$  and  $\lambda = 1$ . The free energy is plotted next to it on a logarithmic time scale. The system reached its steady state around  $t = 30000$ .

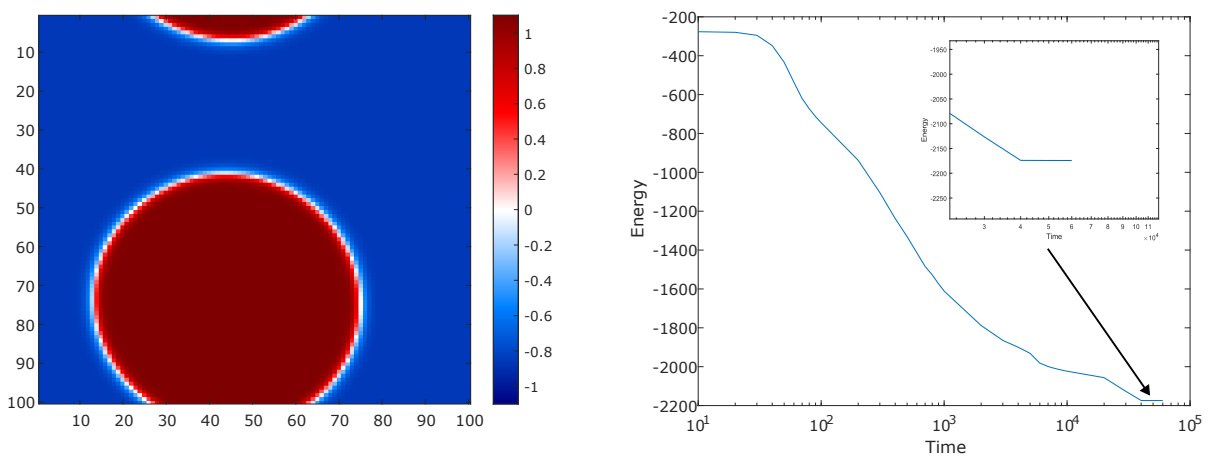


Figure 4.5: System with the same mass and parameters as in Fig 4.4, without solid particles. The free energy is plotted next to it on a logarithmic time scale. The system reached its steady state around  $t = 32000$ .

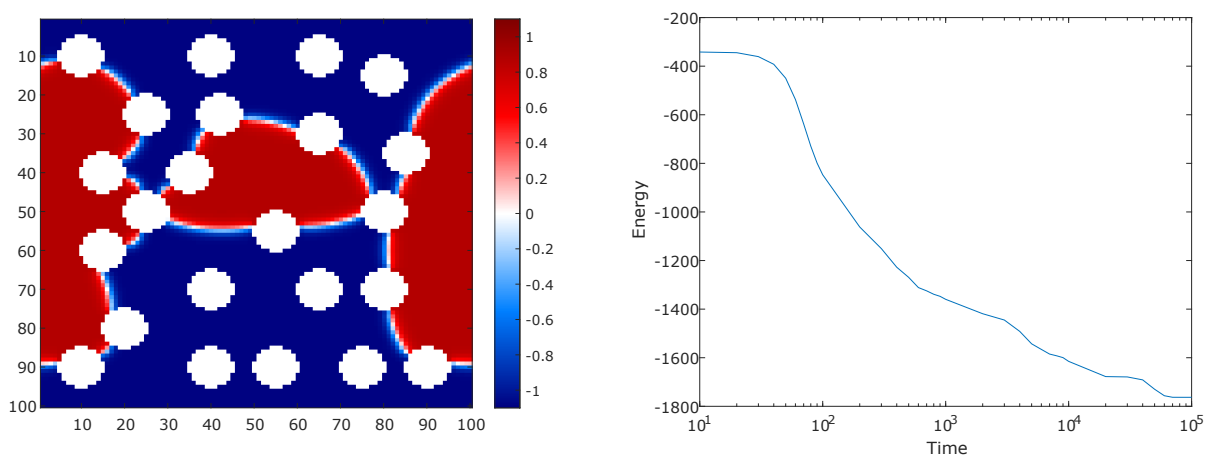


Figure 4.6: System with initial density  $\phi_0 = -0.3$  and  $\lambda = -1$ . The free energy is plotted next to it on a logarithmic time scale. The system reached its steady state around  $t = 80000$ .

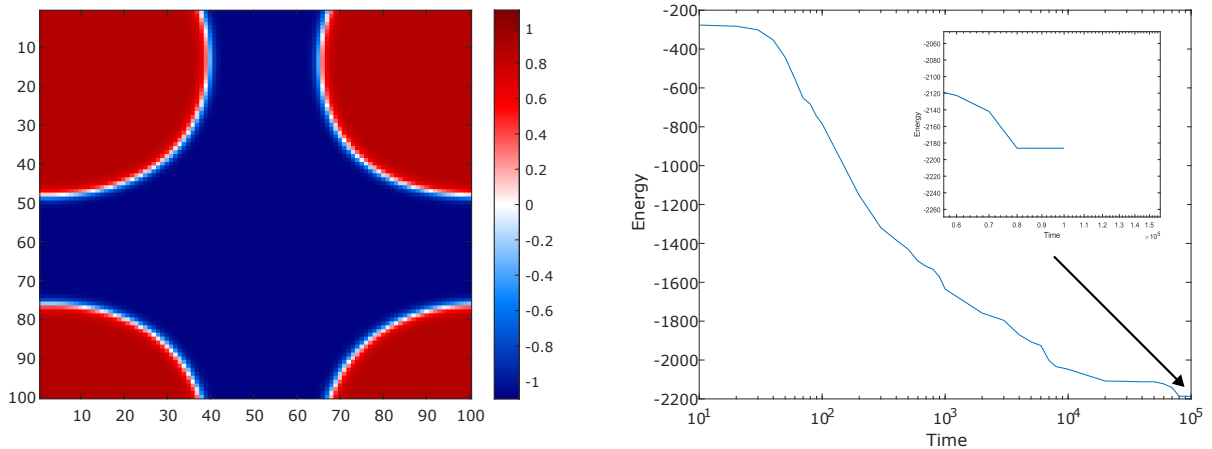


Figure 4.7: System with the same mass and parameters as in Fig ??, without solid particles. The free energy is plotted next to it on a logarithmic time scale. The system reached its steady state around  $t = 80000$ .

Consistently, the system underwent Ostwald ripening, up to a stop, as the clusters were arrested by the solid particles. We thus arrived at a steady state of mesoscopic Ostwald ripening.

Notably, the free energy was initially lower within the heterogeneous topography, but does not reach the same low level in the late stages of development. The systems also reached a steady state around the same time in both topographies.

### 4.3 Simulation of a passive system with noise

Our next step was adding noise to the system by setting  $D = 0.1$ . We took snapshots of the systems at various stages of development to illustrate how the system evolves in time.

We first wanted to analyze how PMB would behave in the heterogeneous topography with noise. We did this to observe how a general phase-separated fluid would behave and compare it to the active case. We simulated a system with initial density  $\phi_0 = -0.3$  and  $D = 0.1$ .

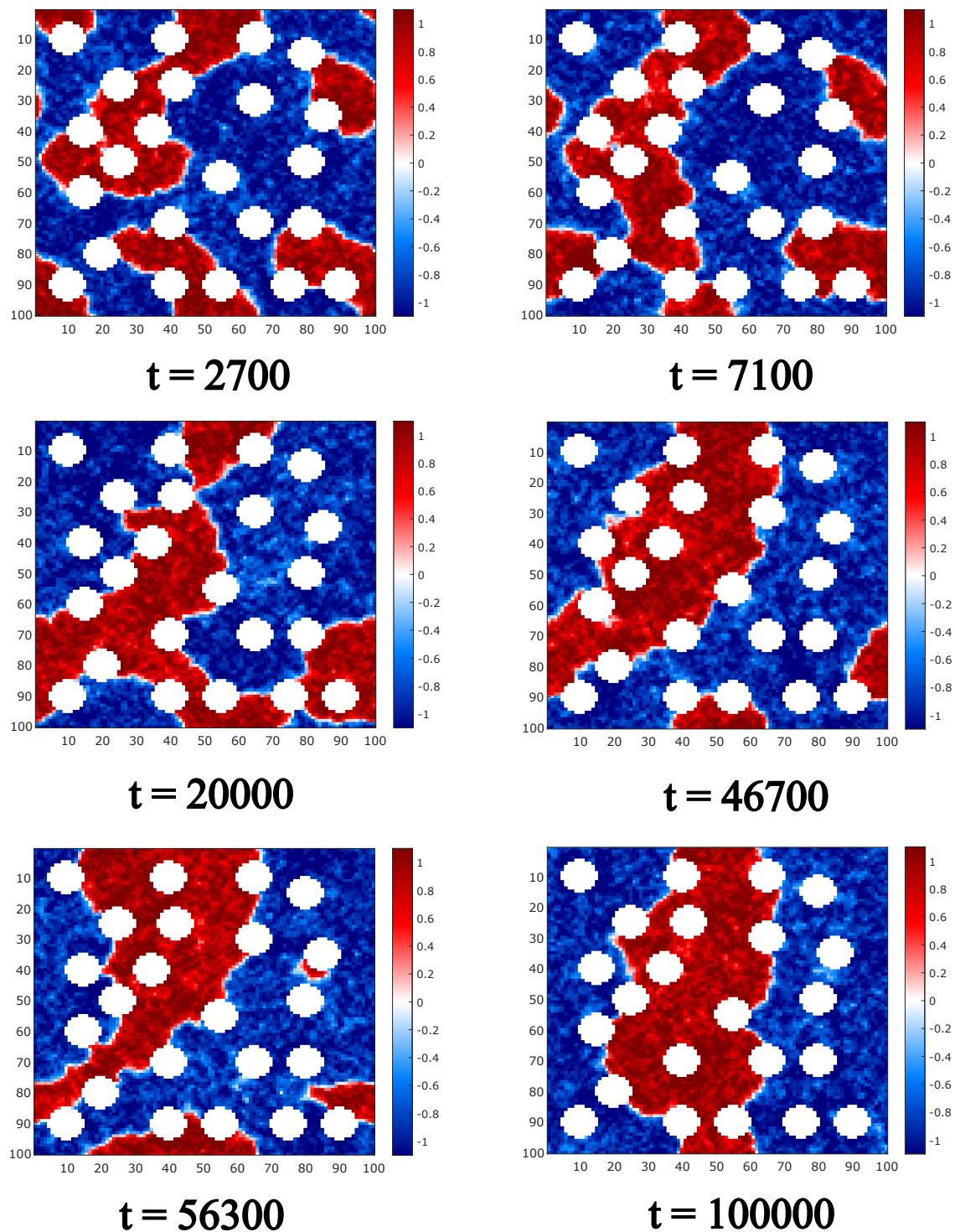


Figure 4.8: System with initial density  $\phi_0 = -0.3$  and  $\lambda = 0$ . The simulation lasted until  $t = 100000$ . We observed Ostwald ripening of the dense phase. The droplet would take shape according to the topography rather than the normal round shape it would take in a homogeneous topography.

The free energy developed like this.

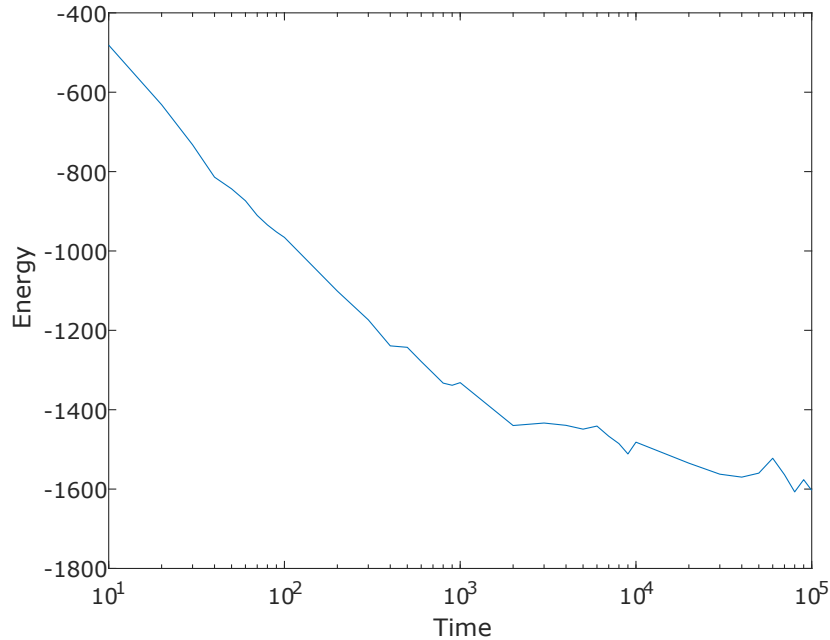


Figure 4.9: Free energy of the above system.

We observed Ostwald ripening, but which faced obstacles forming around the solid particles. A key finding was that the clusters adhere to the solid particles, attaining an elongated shape as it made contact with them. The final large cluster would also take shape according to the topography, as opposed to the standard round shape it would assume in the homogeneous topography.

Notably, with noise, the system would eventually reach a steady state consisting of a single large cluster, as opposed to the numerous clusters we arrive at when noise is absent. The Ostwald ripening dynamic was thus largely restored as to what would happen in a homogeneous topography.

#### 4.4 Simulation with weak activity and noise

Next, we added activity by setting  $\lambda = 1$ , keeping the remaining parameters at their previous levels. The below plots illustrate the behavior we observed

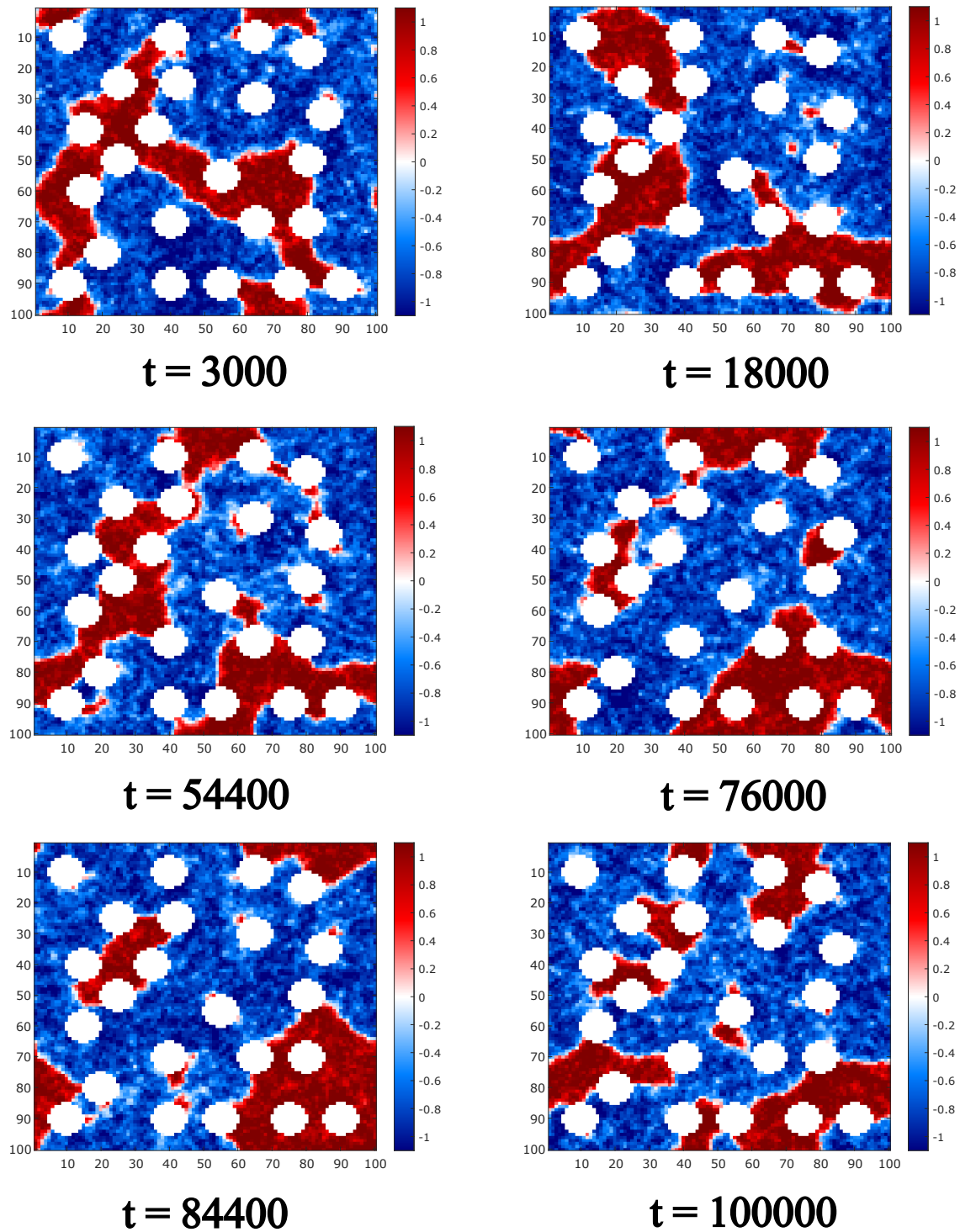


Figure 4.10: System with initial density  $\phi_0 = -0.3$  and  $\lambda = 1$ . The simulation lasted until  $t = 100000$ . We observed that the clusters became more prone to tearing and moving across the lattice than in the passive case. We also observed that the solid particles tended to arrest the clusters forming.

Below is a plot of the free energy development.

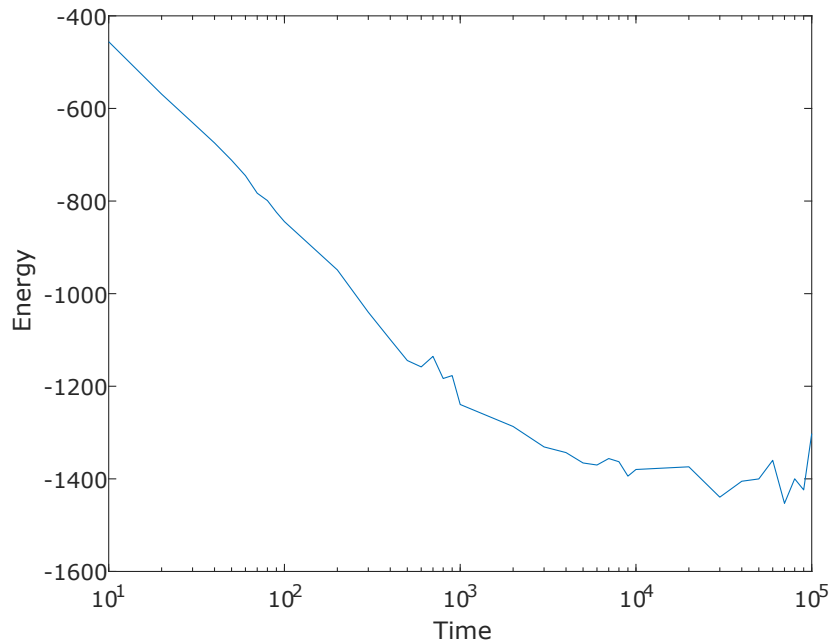


Figure 4.11: Free energy of the above system.

To determine if the system had entered a steady state, we looked at the free energy evolution from  $t = 20000$  to  $t = 100000$ , plotted here using a time-step of  $\Delta t = 1000$ .

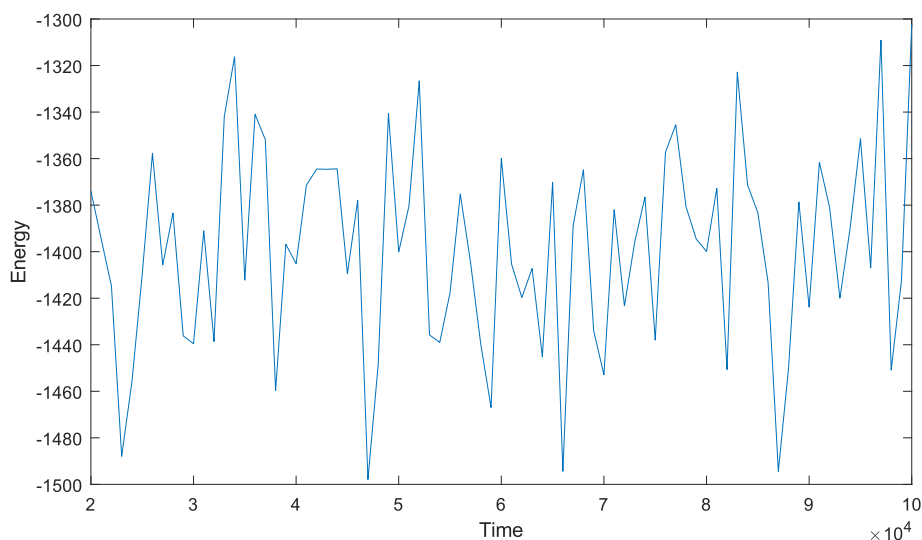


Figure 4.12: Free energy of the above system from  $t = 20000$  to  $t = 100000$ , using a time-step of  $\Delta t = 1000$

Over this period, the system's free energy appeared to oscillate around a mean value of  $-1400$ , indicating a steady state oscillating around a minimal free energy. To test this out, we calculated the mean of the free energy for the two periods  $t = 20000 \rightarrow t = 60000$  and  $t = 60000 \rightarrow t = 100000$ . If these values were considerably close, it would indicate that the system did not change substantially in terms of free energy for a long time, indicating a steady state.

Respectively, these were  $-1396.53$  and  $-1405.04$ . Being so close in values, we propose this to be the system's steady state.

Like in PMB, the system underwent Ostwald ripening, eventually aggregating most, if not all, the active matter in a cluster shaped by the topography. However, we observed several noteworthy changes in the active case.

Firstly, it became difficult to predict where the active matter would aggregate. In the case of PMB, one could determine relatively early where the dense phase would eventually aggregate. As the Ostwald ripening mechanics causes large clusters to grow at the expense of small ones, the final position of the main droplet would usually be placed wherever a large cluster formed early on as a result of the initial conditions.

For example, in the previous plot of PMB in Fig 4.10, one would see early on that the most prominent cluster forms on the left-middle side of the lattice. Based on this, one can predict that the active matter would aggregate around this area.

We also observe a large aggregate in the same area for AMB with  $\lambda = 1$  early on. However, the main cluster ends up in the lower right, and extending through to the upper middle area.

The  $\lambda$  term's effect was moving the clusters across the lattice. Pieces of the aggregates would extend, latch onto the solid particles and drag the aggregates to new positions. This dynamic, in turn, altered the rate at which the Ostwald ripening occurred, as the position where the active matter aggregated was changing.

We also observed that the  $\lambda$  term made the cluster wobble, often shaking off pieces of active matter, which ended up escaping the large clusters and moving away across the lattice.

Another key finding was that certain droplets would also be arrested, unable to join the larger cluster for extended periods. We can observe this in the system at  $t = 54400$ , where there is a large cluster on the system's left side between  $x = 20$  and  $x = 30$ . Most of this cluster eventually migrates upward and to the lower-right side. However, a small portion of the droplet is left stranded between  $y = 20$  and  $y = 50$ .

## 4.5 Simulation with strong activity and noise

Our next step was increasing  $\lambda$  term to 2 while keeping the previous parameters. Because of the dynamics we observed, it was more appropriate to use numerous snapshots of the fluid to make the development understandable. The below plots illustrate the behavior we observed.

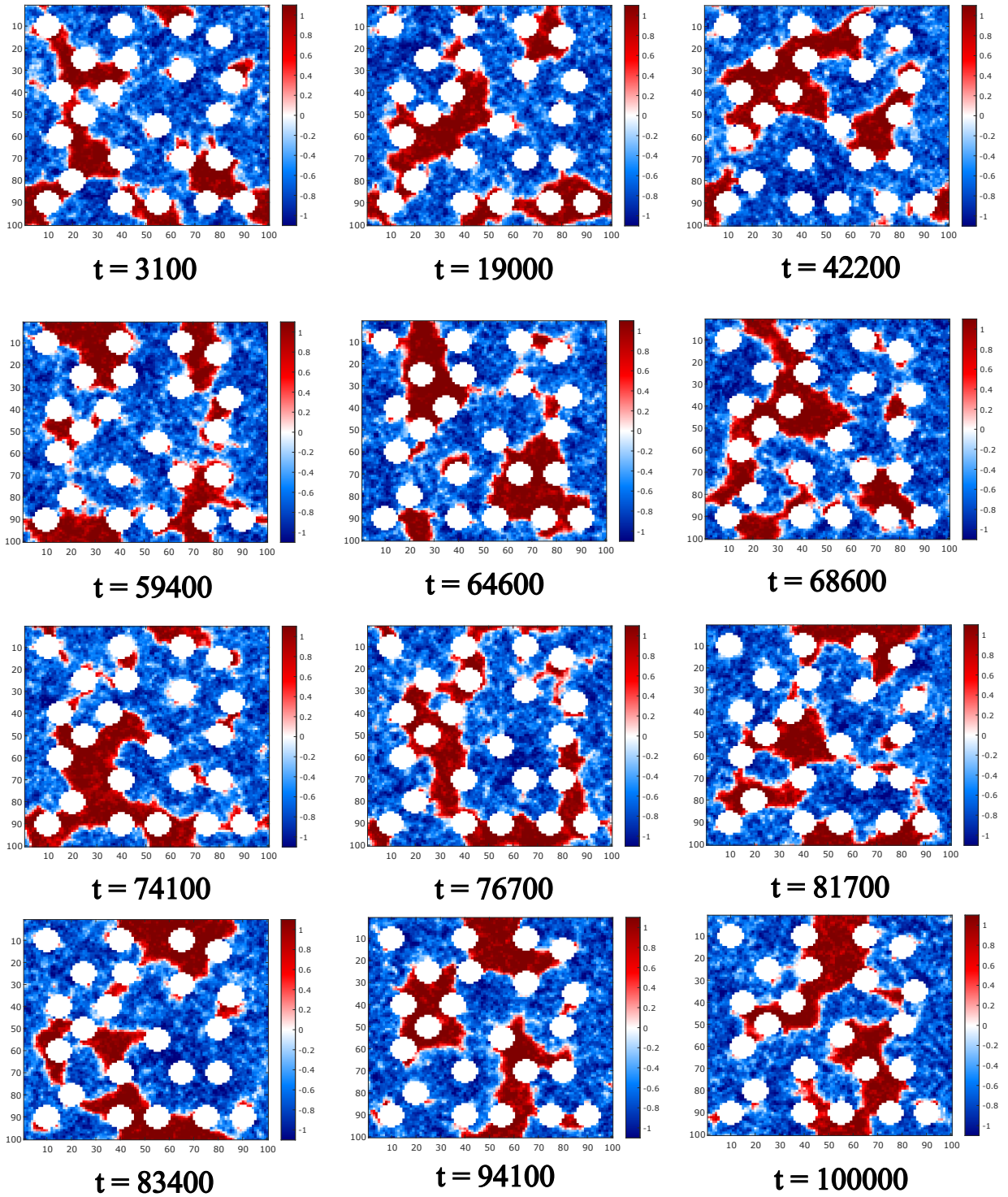


Figure 4.13: System with initial density  $\phi_0 = -0.3$  and  $\lambda = 2$ . The simulation lasted until  $t = 100000$ . Compared to cases of  $\lambda = 1$ , the droplets were more prone to tearing and moving across the lattice. In our simulations with  $\lambda = 1$ , the main cluster would eventually settle down in a location, occasionally wobbling and losing parts. With  $\lambda = 2$ , the main cluster never settled down, constantly tearing apart and reforming while also shifting location

The free energy developed as illustrated below.

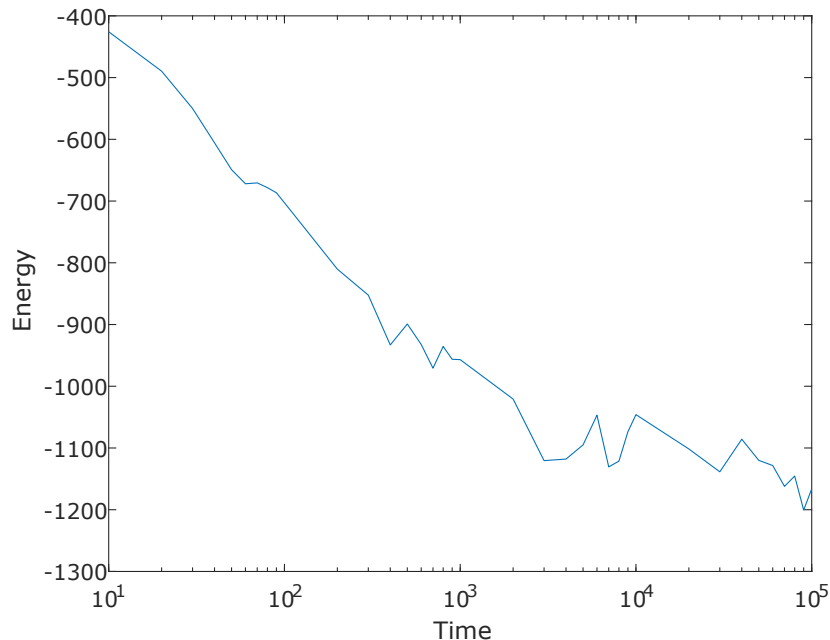


Figure 4.14: System with initial density  $\phi_0 = -0.3$  and  $\lambda = 1$ . The free energy is plotted next to it on a logarithmic scale. The simulation lasted until  $t = 100000$ . We observed that the clusters became more prone to tearing and moving across the lattice than in the passive case. We also observed that clusters tended to arrest amongst solid particles rather than join into the bulk clusters.

Compared to the cases of  $\lambda = 1$ , the aggregation process changed immensely when  $\lambda = 2$ . In the previous case, the main cluster would eventually settle down in a location. It would occasionally lose pieces but remain in one area on the lattice. We can see this in the previous illustration, where most of the time, the main cluster remains in the lower-right corner. However, in the case of  $\lambda = 2$ , the main cluster constantly changed position.

Furthermore, the division we observed previously grew far stronger. Large clusters would occasionally emerge, as seen in the upper right portion of the lattice. However, these clusters would all inevitably dissolve, before reemerging elsewhere. These would also dissolve, and the main cluster would again reemerge elsewhere, sometimes at its original position, in a seemingly endless cycle of death and rebirth. Because of this, we let the simulation time out at  $t = 100000$ .

We remarked that the dynamics observed in the  $\lambda = 2$  experiments were similar to the ones modeled by AMB+, which involves the bulk being torn apart into smaller portions. The heterogeneous topography appeared to instill a form of reversed Ostwald ripening into the

To determine if the system had entered a steady state, we looked at the free energy evolution from  $t = 20000$  to  $t = 100000$ , plotted here using a time-step of  $\Delta t = 1000$ .

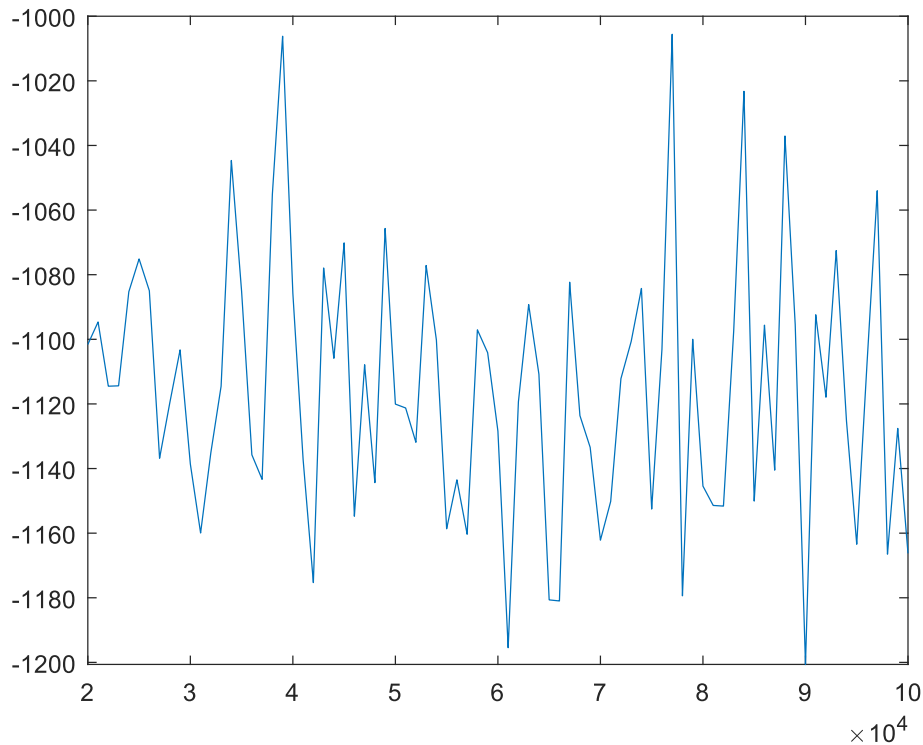


Figure 4.15: Free energy of the above system from  $t = 20000$  to  $t = 100000$ , using a time-step of  $\Delta t = 1000$

Over this period, the system's free energy appeared to oscillate around a mean value of -1120, indicating a steady state oscillating around a minimal free energy. Because the steady state appeared to involve reverse Ostwald ripening, we decided to create a system with an initial state consisting of a large cluster surrounded by the dilute phase. This state would be reasonably stable. As such, if the  $\lambda = 2$  system would eventually reach a steady state with a single large cluster as in a homogeneous topography, we expected this new system to not change much from its initial state.

## 4.6 Simulation with initial stable state and activity

We created an initial state with a large cluster of active matter having already aggregated and observed how it changed.

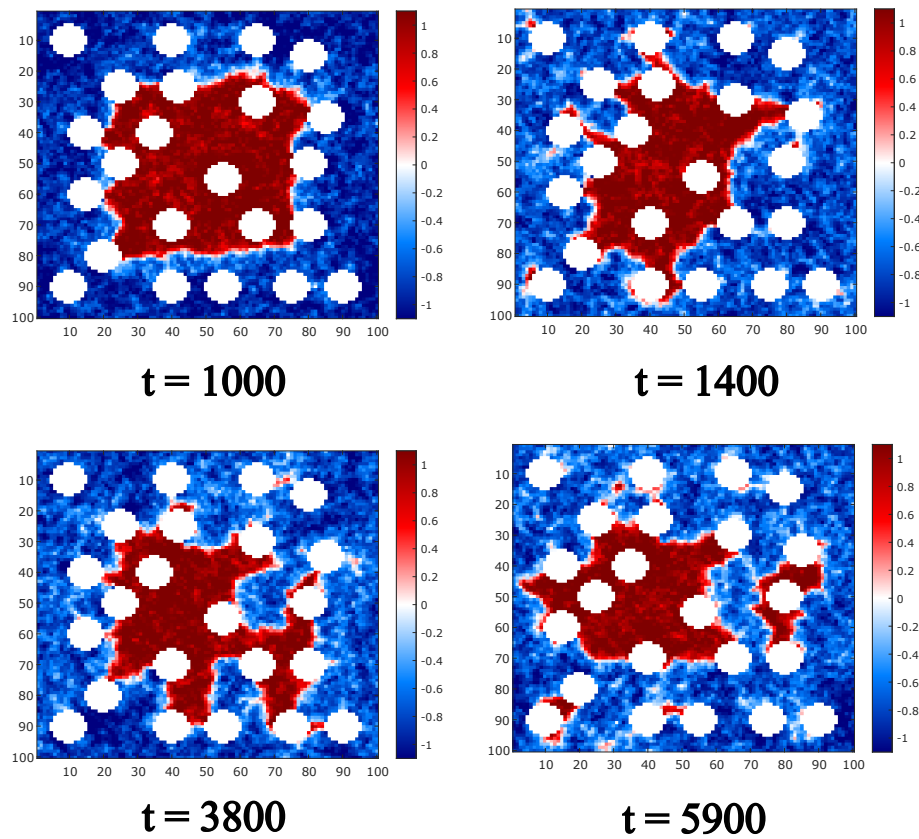


Figure 4.16: Initially stable system with  $\lambda = 2$ . The cluster soon start dividing.

We observed that the cluster quickly spread out. Tendrils emerged from the cluster that latched onto solid particles. This caused the cluster's shape to change, eventually making it lose segments.

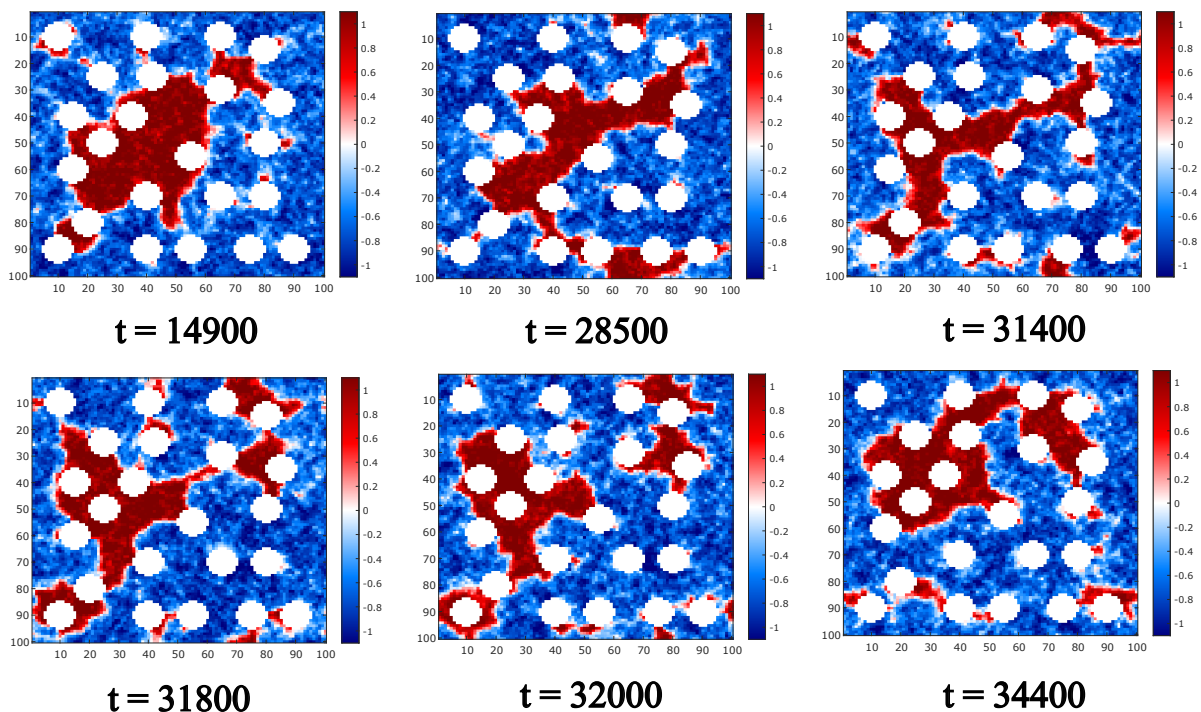


Figure 4.17: Initially stable system with  $\lambda = 2$ . We observe that the cluster quickly spreads out and divides.

The cluster would become elongated, stretching out to contact numerous nodes. A pivotal development emerged in the sequence starting at  $t = 31400$ . The elongated droplet is

stretched thin at  $t = 31800$  before breaking at  $t = 32000$ . As a result, the droplet divided, before reforming again at  $t = 34400$

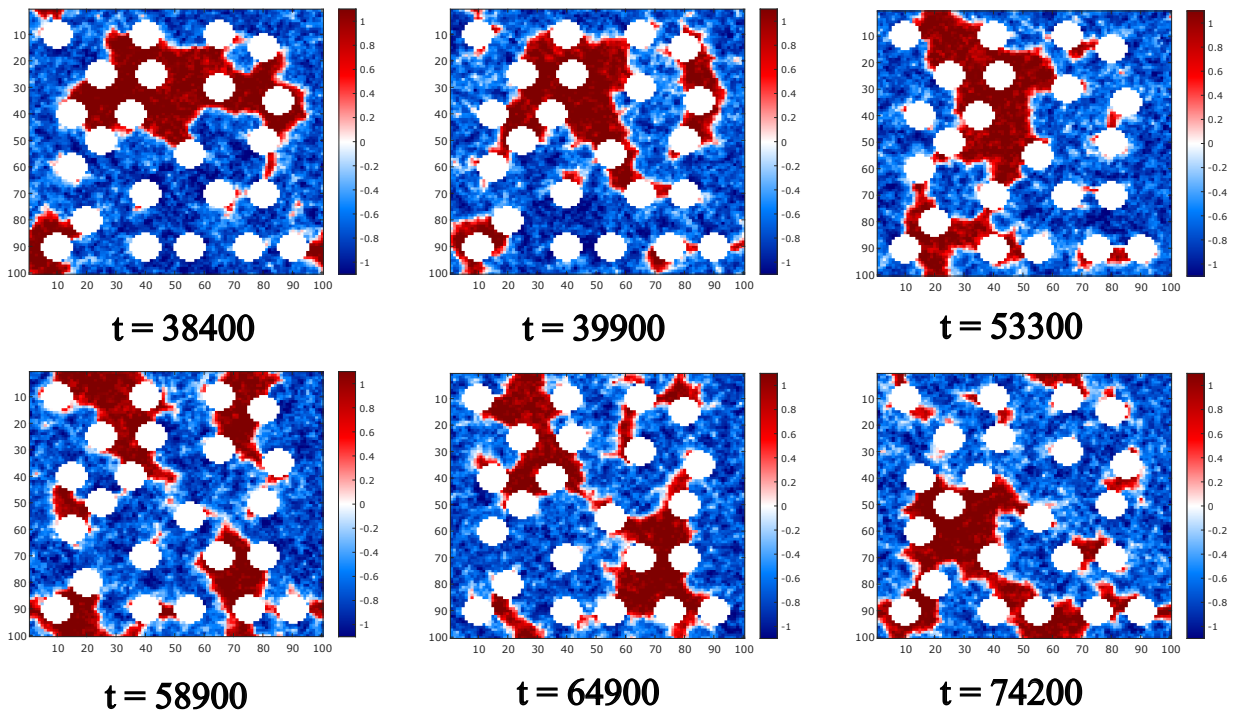


Figure 4.18: Initially stable system with  $\lambda = 2$ . The simulation lasted until  $t = 100000$ . The largest cluster repeatedly changes position

The dynamics continued at  $t = 38400$ , where the cluster had migrated upwards and reformed. Then at  $t = 39900$ , it divided again. Leading up to  $t = 64900$ , the cluster divided into two almost equal droplets that again reform at a new location.

The free energy of the system developed as follows.

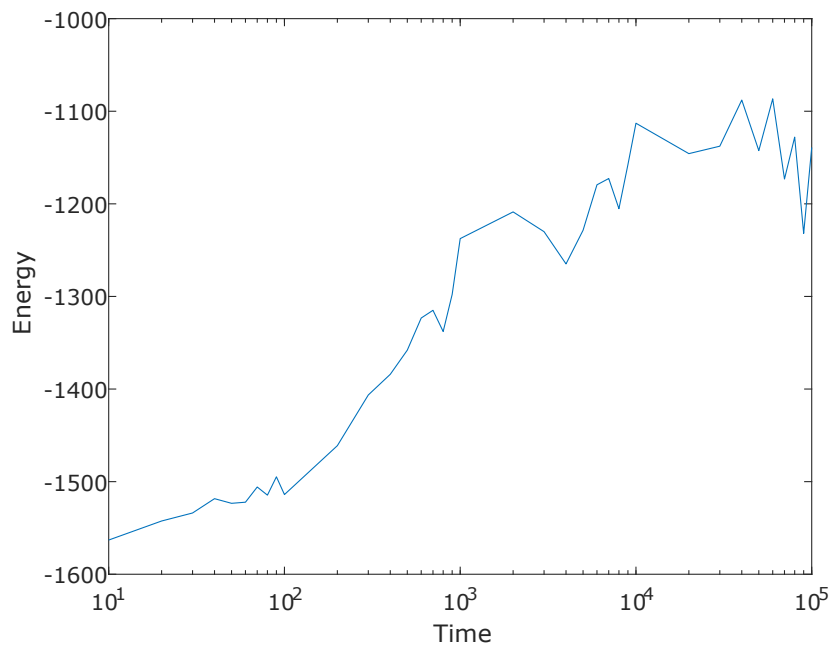


Figure 4.19: Free energy of the above system.

Unlike the previous examples, the free energy rose in the early stages of development, indicating reverse Ostwald ripening.

To determine if this chaotic dynamic was the system's steady state, we calculated the mean free energy of both this system and the one in the previous section  $t = 20000$ , that being the time the reverse Ostwald ripening began. In both cases, our qualitative analysis led us to believe this was the time when the chaotic dynamic emerged in both systems.

The final stage free energy mean for the initially homogeneous system was  $-1117.70$ . The system starting from a large cluster had a final stage free energy mean of  $-1113.50$ . This finding strongly supports the proposal that the active systems' steady state is the continuous, chaotic destruction and reemergence of clusters.

In both the cases where we started with a uniform density and the one where we started with an aggregate, we observed the same qualitative and quantitative behavior. The active matter would aggregate and divide in cycles. The fact that it diverged from the stable initial state indicated that the system might never reach a final stable state. As such, we decided not to continue the simulation to see if such a state could be achieved.

## 4.7 Simulation with negative activity

Our experiments so far involved a positive  $\lambda$  value. We also thought it would be worthwhile to study what kind of dynamic we attained when  $\lambda < 0$ . As we had observed the dynamics of the system changing massively for  $\lambda = 2$ , we decided to make a simulation using  $\lambda = -2$ . This value would grow the dense phase. Wanting to keep the total area of the active clusters relatively close to our previous experiments, we reduced the initial density to  $\phi_0 = -0.4$ .

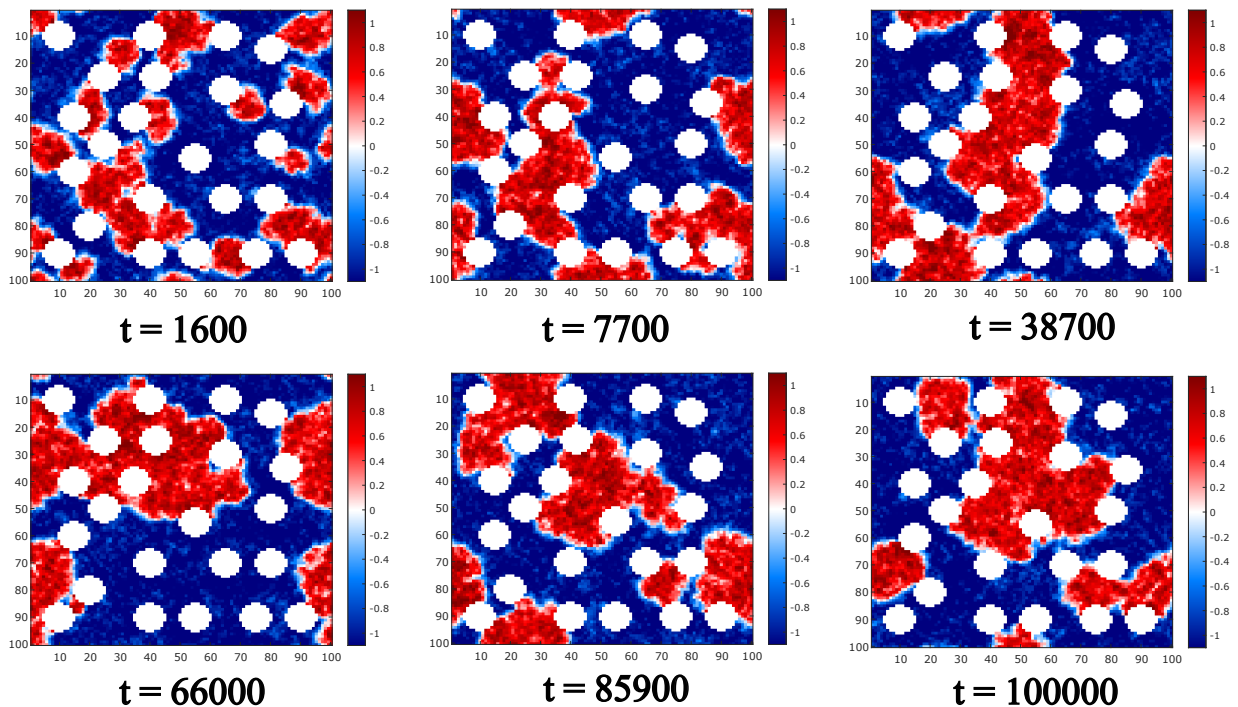


Figure 4.20: System with initial density  $\phi_0 = -0.4$  and  $\lambda = -2$ . The simulation lasted until  $t = 100000$ . We observed a great degree of Ostwald ripening. Droplets tended to aggregate within collectives of solid particles, which also served as obstacles, occasionally causing tears in the droplets.

The free energy of the system developed as follows.

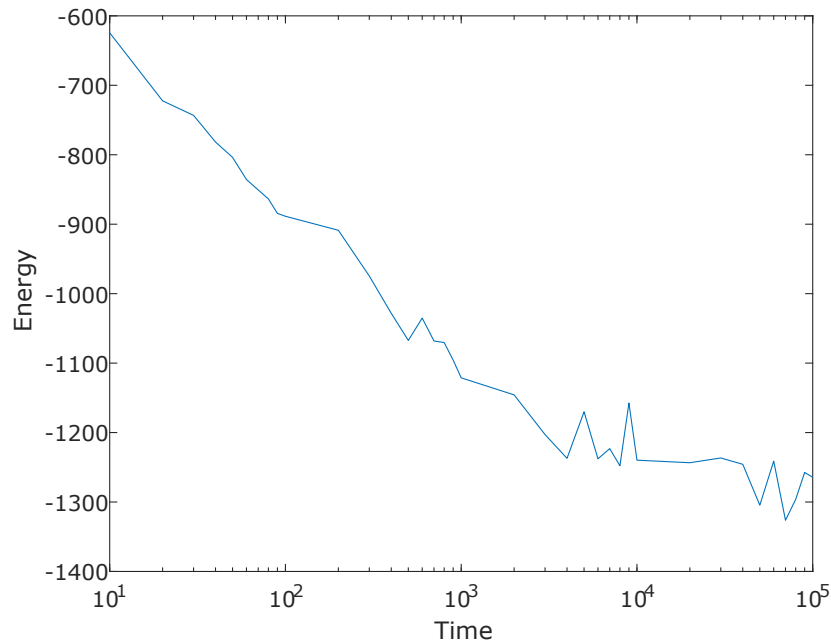


Figure 4.21: Free energy of the system above.

Again we observed a different dynamic. With this negative parameter, Ostwald ripening was largely restored. The clusters soon aggregated into a large cluster. While the clusters would occasionally lose portions, they could aggregate into a single large cluster and remain intact for long periods.

To determine if the system had entered a steady state, we looked at the free energy evolution from  $t = 20000$  to  $t = 100000$ , plotted here using a time-step of  $\Delta t = 1000$ .

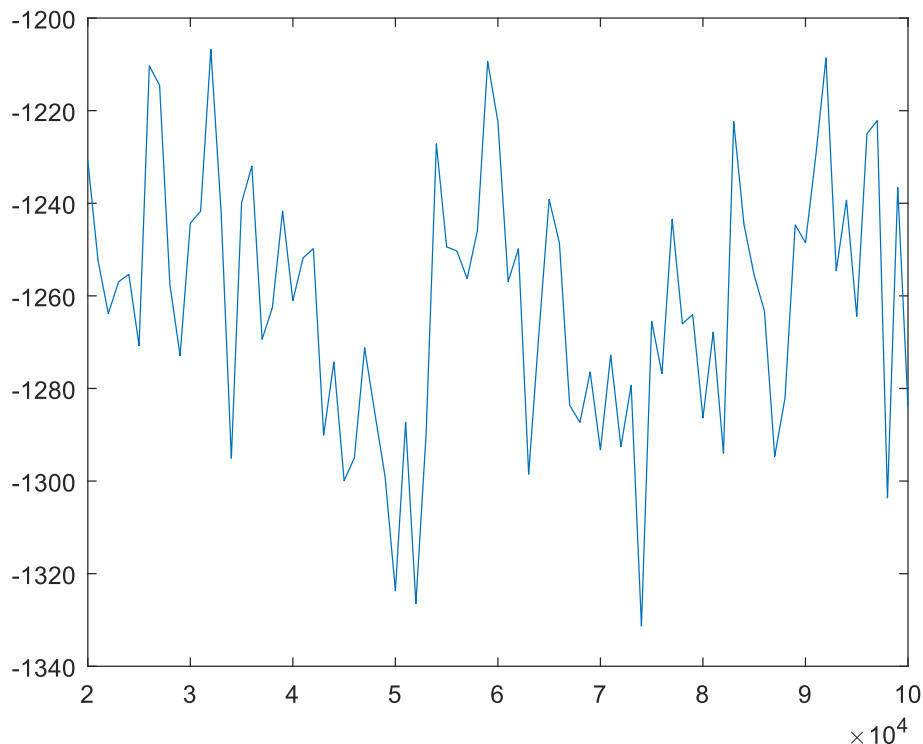


Figure 4.22: Free energy of the above system.

Over this period, the system's free energy oscillated around a mean value of 1270. To test this out, we calculated the mean of the free energy for the two periods  $t = 20000 \rightarrow t = 60000$  and  $t = 60000 \rightarrow t = 100000$ . If these values were considerably close, it would indicate that

the system did not change substantially in terms of free energy for a long time, indicating a steady state.

Respectively, these were -1275.64 and -1264.29. Being so close in values, we propose this is the system's steady state.

## 4.8 Additional experiment: Simulation with partially-homogeneous and partially-heterogeneous topography.

We noted that the active matter tended to aggregate more often at the left side of the  $\Omega_{main}$ . What is noteworthy about the left side of  $\Omega_{main}$  is that it has a higher density of solid particles. Thus, we postulated that the active matter preferred residing within a dense, heterogeneous topography.

To test this out, we created a system where we removed all solid particles on the left side of the lattice. This produced the following development.

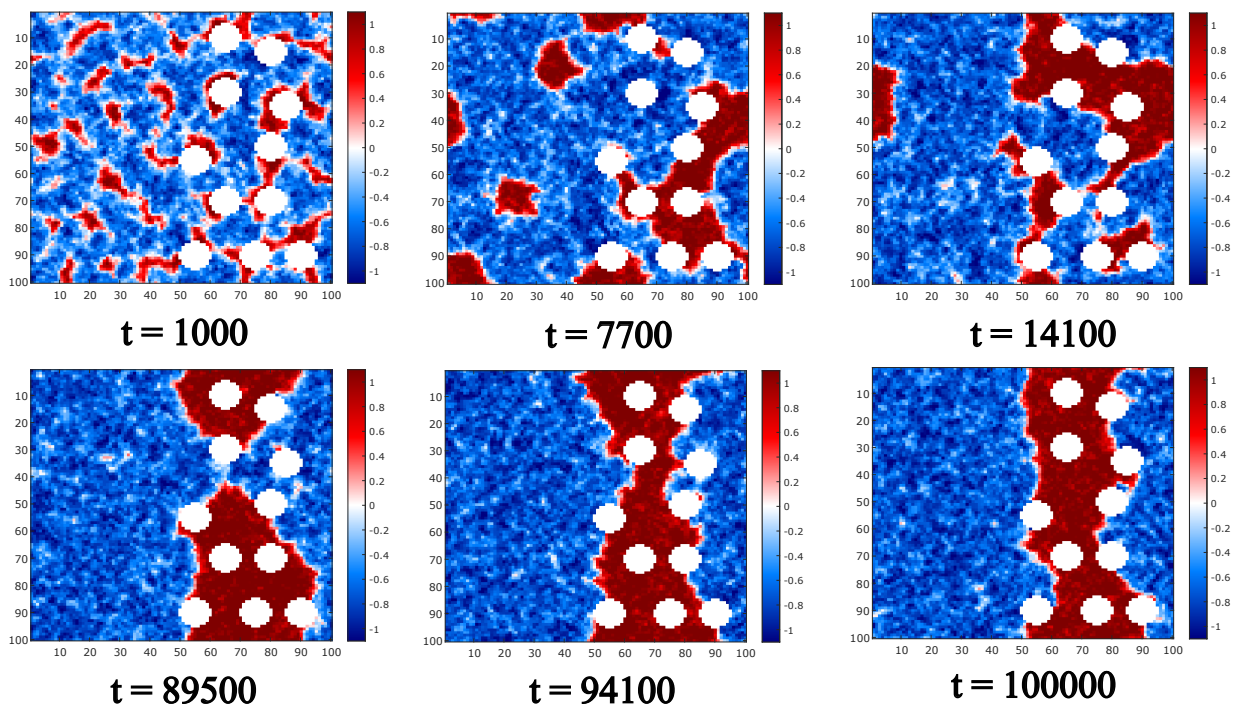


Figure 4.23: System with total mass  $\sum_{i,j}\phi_0 = -0.3$  and  $\lambda = 2$ . The simulation lasted until  $t = 100000$ .

The active matter did indeed aggregate around the solid particles. Unlike the previous, we arrived at a seemingly stable state with a single large cluster. With this topography, the active matter behaved more like PMB, aggregating around the solid particles and immersing them without division or tearing.

## 4.9 General results

| Observed behaviour       |  |                              |
|--------------------------|--|------------------------------|
| Heterogeneous topography | Noise Present  | No Absent                    |
| Active system            | Mesoscopic, or reverse Ostwald ripening depending on active parameter value. | Mesoscopic Ostwald ripening. |
| Passive system           | Macroscopic Ostwald ripening.  | Mesoscopic Ostwald ripening. |

# Chapter 5

## Discussion

### 5.1 Interaction between active and solid matter

In our simulation, we observed several similarities between the active matter modeled by AMB and the behavior of *M.Xanthus* in a heterogeneous topography[2]. A key similarity was that active matter would adhere to the surface of the solid particles, similar to how the *M.Xanthus* bacteria would adhere to silica particles[2]. The active matter would do this, as adhering to solid particles would remove sections of the phase-separated interface, which is thermodynamically preferable for the system. Conversely, letting go of a solid particle would result in the formation of an interface, which would violate the thermodynamic development of the system. This adhesion would, in turn, significantly alter the system's dynamics.

When noise was absent, we observed that the active matter would aggregate as it would in homogeneous topography, but only on a mesoscopic level. One notable difference was that the active matter would usually aggregate near solid particles, generally fitting into groups of solid particles. This aggregation dynamic emerges due to the thermodynamic feasibility of adhering to solid surfaces. As a result, the active droplets preferred locations surrounded by solid particles. We observed this directly by having solid particles on the right side of the lattice, causing all the active matter to move to that side.

Notably, certain bodies would have interfaces bulging out between two solid objects. This phenomenon seems counter-intuitive, as the interface would be shorter if it were a straight line. We attribute this phenomenon to the system balancing free energy reduction and mass conservation. Though the system seeks to minimize its interface, the clusters still have finite sizes that must fit within the collectives of solid particles. The bulges emerge as part of the clusters are "spilling out" as they attempt to fit into the solid particle sets. As a result, the clusters tended to be more elongated within the heterogeneous topography, stretching out to fit in with the topography.

## 5.2 The effect of Heterogeneous topography on Ostwald ripening

A notable change in the dynamics imposed by the topography, as opposed to the homogeneous case, was that the Ostwald ripening would eventually halt. Rather than each phase constituting a single body each, the two phases would gather into several disparate bodies. Once the active clusters found a stable position among the solid objects, they usually ceased joining with others. The noiseless systems would thus reach a final state of mesoscopic Ostwald ripening. This conclusion is supported by the fact that the free energy would eventually cease decreasing along with the droplets ceasing to grow.

We attribute this to clusters finding local free energy minima amongst the solid particles. Once a cluster adheres to several solid particles, it becomes exceedingly difficult for them to let go, as doing so will create a phase-separation interface, increasing the free energy, which violates the thermodynamics of the system. The clusters are thus most stable when they remain arrested between the solid particles. This arrest leaves them no explicit reason to move, as doing so would incur free energy costs. Furthermore, the clusters did not dissipate as they would normally. To accomplish this, the interfaces would have to curve inward on the clusters themselves. Doing so would also increase the interface's length, making this process impossible.

Notably, the system's free energy could still be reduced globally if all the clusters joined together. Even so, each cluster is trapped in a local free-energy minimum. Thus they cease to aggregate further, preventing global free energy from reaching a minimum. The dynamics of the phase separated fluid in a heterogeneous topography are driven by the system minimizing local free energy at the cost of being unable to minimize global free energy. We can observe this quantitatively in Section 4.2, where the free energy in the heterogeneous topography never reaches the low levels it would in the homogeneous topography. We end up with an arrested development, similar to what was observed in the paper by Ramos et al[2].

In the cases where we did not have noise in our system, the time to the steady state was almost the same in both a homogeneous topography and a heterogeneous topography. We made this discovery relatively late. As such we did not invest time in seeing if there was a symmetry for the times until the systems reached their individual steady states. We thus do not know if there is any physical significance to this and suppose it could be coincidental.

## 5.3 Dynamics with noise

The system's dynamics would change drastically again when we added noise. The noise added isothermal energy to the system, perturbing the clusters and making it more difficult for them to adhere to surfaces permanently. Consequently, clusters would not necessarily be arrested between solid particles as they would in the simulations without noise. As a result, arrested clusters could find to escape their local free energy minima, which in turn meant aggregation could continue until all the active matter had aggregated, and a global minimum was achieved.

In PMB, the system would usually reach a steady state where it minimized free energy

through a compromise between adhering to the solid particles and Ostwald ripening. The system would aggregate each phase into a singular cluster, which would take shape according to the topography. Based on the mechanics of the Cahn-Hilliard Neumann problem, this dynamic is what we expected to see.

Conversely, AMB behaved very differently. Depending on how many solid particles we placed into the topography, the system never reached a state with a single large stable cluster. For small values of the  $\lambda$  parameter, we would still observe some degree of normal Ostwald ripening, with the solid particles acting like obstacles and occasionally tearing pieces of the clusters that were stuck.

The dynamics changed drastically when we increased  $\lambda$  to 2. Clusters would form, only to be torn apart and dissipate. We often observed aggregation in one area of the lattice, only for the cluster to disappear and reappear in a completely different location. This dynamic came as a surprise, as previous literature on AMB reported the model was qualitatively similar to PMB, doing little more than altering the binodal densities and shape of the clusters[3].

This new dynamic emerged because of conflict in the manner the system had to minimize its free energy. We showed that if the bulk size were about the same as the area covered by solid particles, AMB would behave much like PMB, covering the active particles in a single cluster. Once the area covered by the solid particles exceeded that of the active matter, it would start to divide. This is because the topography creates multiple regions where clusters can attain a local free energy minimum through Ostwald ripening in that region.

As we showed in our first simulation, the dynamics of a phase-separated fluid by clusters evolving toward local free energy minima rather than the whole system moving to a global minimum. The processes whereby clusters achieve local free energy minima conflicted, as one process involved pulling the cluster in one direction. In contrast, the other process pulled the cluster in another direction. We see this in 4.17, specified below in figure 5.1.

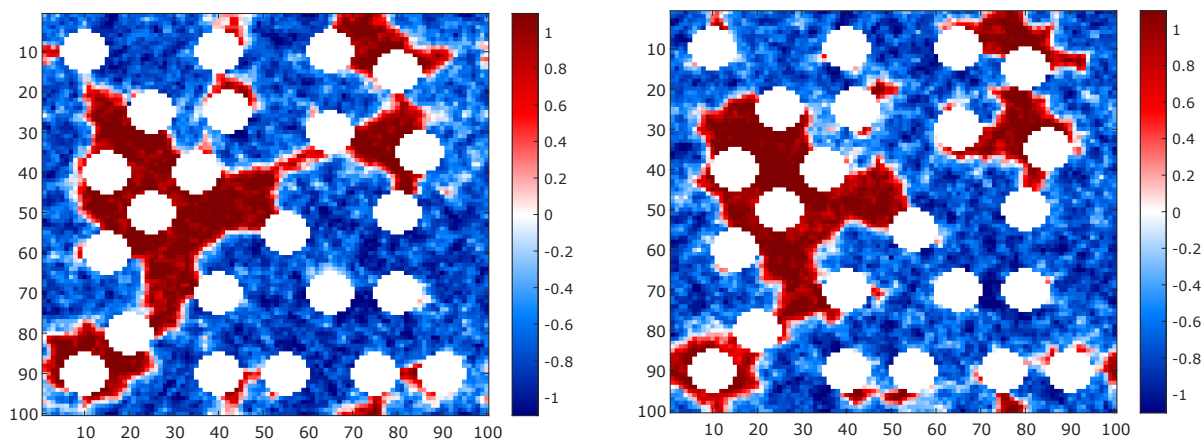


Figure 5.1: The cluster is torn apart by competing Ostwald ripening events.

In PMB, the clusters would find a balance between conflicting dynamics, even when the area covered by particles exceeded that of the bulk. In AMB, however, what emerged was a sort of tug-o-war between the parts of the large clusters, both trying to pull the rest of the cluster closer. This conflict would often, if not always, result in clusters tearing apart. Large clusters were thus divided into smaller ones.

The Ostwald ripening dynamics of the system entail that small clusters disappear while large ones grow[4]. As a result, clusters that had grown considerably due to Ostwald ripening could suddenly lose a significant amount of mass, leading to dissipation and eventually causing them to disappear altogether. The matter that constituted it would travel elsewhere and aggregate before repeating the process. This behavior was further enabled by the elongation imposed by the topography, making it easier for parts of the clusters to extend and break away from the main body.

## 5.4 The effect of $\lambda$

The obvious question is why this occurs. The behavior change must be caused by the active  $\lambda|\nabla\phi|^2$  term coupled with the Neumann boundaries. The purpose of the active term is to model quorum sensing[4], i.e., the ability of active matter constituents to detect the nearby behavior of active matter. Specifically, AMB allows the active matter particles to detect nearby gradients[3]. This term then alters the growth rate of  $\phi$  near the interface from the passive case. The active matter near the interface will thus attain a density that differs from the passive case. As the system aims to erase gradients, the rest of the phase will attain the same density in a ripple effect, propagating inwards. Thus, AMB models actively seek to lower the system's free energy by changing the binodal densities and, thus, the size of the droplets.

We showed that when active matter clusters impact solid surfaces, they will naturally adhere to them. Due to the quorum sensing, this event will be detected by particles deeper into the droplet. As adhering to a solid surface is thermodynamically beneficial, the clusters will actively seek to undergo Ostwald ripening at the surface. However, this information is not communicated throughout the entire cluster. The cluster portions far away from a solid particle do not detect a solid surface. If it instead detects another surface, it will instead actively attempt to reduce the free energy at the latter.

As previously mentioned, these can conflict if the area covered by the particles exceeds that of the droplets. While PMB can strike a balance with such conflicting processes, the active fluid portions will seek to reduce local free energy far more rapidly, irrespective of how the rest of the cluster behaves. These disparate events create tension within the clusters that ultimately tear the clusters apart. This, in turn, causes a phase-separation interface to emerge. We observe this behavior in Figure.5.1, as two parts of clusters, each immersed in a set of active particles, cannot compromise on where to aggregate, instead seeking to drag the rest of the cluster to their location.

These findings indicate that the quorum sensing modeled by AMB has a limited range, meaning information is not communicated throughout the cluster. This result also illustrates a property of active matter: though they have collective behavior, individual particles can behave independently. In turn, sub-collectives of active matter can also make independent decisions. In our case, sub-collectives will attempt to minimize the free energy locally, which ends up increasing the free energy globally.

The observed dynamic shares several similarities with AMB+, a model which also makes large cluster tear and divide. Notably, AMB+ models reverse Ostwald ripening occurring due to the natural chemical properties of the fluid[4], whereas our system divides droplets due

to internal conflict imposed by the topography. However, one key similarity lies in how both minimize free energy. AMB+ limits the size of clusters. Any cluster that goes above this threshold begins dissipating or dividing. Effectively, AMB+ minimizes free energy locally. This is also thermodynamic that drives our system.

This dynamic is quite ironic. By attempting to decrease the free energy of individual aggregates, the active matter ends up increasing its free energy. This is why these simulations never seemed to reach a stable state. The system undergoes transient periods of free-energy decay, followed by sharp rises of the free energy due to droplets tearing. Because of these phenomena, there is a strong case for the system never reaching a stable state of a single cluster. Notably, this dynamic depends on a constant supply of energy, as the free energy cannot periodically increase forever. In our case, the noise supplies the system with energy, as it constantly perturbs the system, allowing these indefinite thermodynamics. If the noise disappears, the system eventually runs out of free energy, and future developments are arrested, as previously noted.

Of note was that the dynamics were not symmetric with respect to the sign of  $\lambda$ . We only achieved the chaotic dynamics when the sign of  $\lambda$  was positive. Once we used a negative  $\lambda$  value, the reverse Ostwald ripening dynamics diminished notably. When  $\lambda$  was negative, the solid particles acted almost entirely like obstacles, as we had initially imagined. This change could be related to how the quorum sensing modeled by the  $\lambda$  term treats the phases. For the dense phase, a positive  $\lambda$  creates a signal informing the active matter to gather closely, bringing the clusters closer to the solid particles.

Conversely, a negative  $\lambda$  tells the dense phase to spread out. As such, the droplets are not as motivated to aggregate in the close vicinity of solid particles and will instead aggregate in a general neighborhood around them. This means separate clusters will maintain a large degree of contact, and thus they do not interfere with the Ostwald ripening dynamic as much.

## 5.5 Interpretation of the newfound dynamics

These findings surprised us. Our prior simulations of AMB indicated the model was merely quantitatively, not qualitatively, different from a passive phase-separating fluid. We had not expected the topography to alter the system's dynamics on such a fundamental level. We anticipated a dynamic akin to PMB, where the active matter would still aggregate into clusters, only placing gathering in or around the solid particles.

The dynamics of AMB in the heterogeneous topography were highly chaotic and difficult to predict. We would get very different trajectories for the clusters each time. Certain patterns could be observed, however. The clusters tended to assemble at the left side of *main* in repeated cycles. There was rarely any time when the matter was absent from the left side. We attribute this to the fact that it has a higher density of solid particles compared to the right side, which the active matter preferred. As such, one may assume the clusters generally will move to areas with high particle density.

We were also surprised about the similarities between our findings and that of the paper by Ramo et al[2]. Notably, the topography could arrest the aggregates and alter their size and

shape. This discovery makes a strong case that the topography surrounding active matter significantly affects the aggregation process, as found in the said paper[2].

Another key development was that the active term would induce motion into the clusters. By creating a large cluster in the system as the initial condition, we could observe how the active system would behave after becoming an approximately steady state. The cluster would often move, sometimes far away from its initial position, and in several cases, be divided into smaller clusters.

The key finding in the paper by Ramos et al. is that the topography altered the ability of the bacteria to form large clusters[2]. This effect increased with the packing density of the solid particles. This is remarkably similar to what emerged in our simulation. As reducing the number of particles allowed for normal Ostwald ripening to resume.

A notable difference is that the aggregates in said paper tended to keep a relatively round shape[2], while our aggregates tended to be amorphous. The bacteria in that paper also tended to form several medium sized aggregates, rather than one[2]. AMB+, tends to create round aggregates rather than the amorphous ones we saw. It is possible that AMB+ would be a better simulation of the behavior noted. This could also relate to the time-order of the systems. Specifically, the time-steps we used correspond to large periods in the real world. System size, and total mass of active matter could also come into play, as clusters will take longer to aggregate the smaller they are compared to the full system.

## 5.6 Future development

Potential future research could involve simulating the model with higher-order differential operators. As the chaotic dynamics appear to primarily be driven by the limited range of the quorum sensing, using longer-range stencil operators may allow for improved information transmission throughout the droplets, preventing or decreasing the chaos we observed.

We had initially planned to simulate AMB+ in a heterogeneous topography but found challenges in implementing the necessary boundary conditions. AMB+ is dependent on higher-order differential operators to function. Literature about how to implement the required boundary conditions was limited. What little we found tended to be incompatible with our model. We are unsure if we were unlucky in our search or if no one has found ways to implement these boundary conditions. As such, there may be numerous challenges in making a simulation using AMB+, down to simply numerical challenges.

Based on our previous experiments with AMB+, we hypothesize that the topography would not heavily alter the dynamics of AMB+. Due to the nature of AMB+ imposing limits for the size of the droplets, it could, depending on the actual maximal droplet size, likely not experience the tearing we observed in AMB.

Notably, the heterogeneous topography would affect the active matter, so it engaged in an effective reverse Ostwald ripening. Large droplets would, in cases of low activity, move across the lattice. Increasing the active parameter resulted in large droplets dividing, limiting their maximal size. We predict we would observe a dynamic where the droplets adhere to the solid particles but do not join together like in AMB.

We had considered further analyzing the circumstances that lead to the clusters tearing, which we assume would relate to tension within the interface of the clusters. However, the interfacial tension in AMB is still a field of study [19]. With this new dynamic only recently discovered, we thought this task could not be completed. However, our findings may give further insight in the interfacial tension of active phase-separated fluids.

# Chapter 6

## Conclusion

A heterogeneous topography can significantly alter the dynamics of active matter. Beyond merely acting as obstacles, solid particles can arrest the Ostwald ripening of the system or even reverse it.

Ostwald ripening is arrested in the absence of noise perturbations for both passive and active matter in a heterogeneous topography. This emerges because the topography alters the thermodynamics of the system, from minimizing free energy globally, for minimizing it locally.

For passive matter, or negative value of the active  $\lambda$  term, Ostwald ripening still occurs almost as it would within a homogeneous topography, with the solid particles acting mainly as obstacles.

When  $\lambda$  is positive, Ostwald ripening is often arrested. While  $\lambda = 1$ , the clusters still undergo Ostwald ripening and gather into clusters at a mesoscopic scale. Rarely are all clusters able to gather, as several are arrested.

When  $\lambda = 2$ , the Ostwald ripening process reverses. This new dynamic emerges from competing Ostwald ripening events occurring at several locations in the topography. In a heterogeneous topography, active matter dynamics are driven by a tendency to minimize local free energy at the cost of being unable to minimize global free energy.

Consistently, assuming the area covered by the active matter does not exceed that covered by the solid particle, the systems reach a steady state of mesoscopic Ostwald ripening.

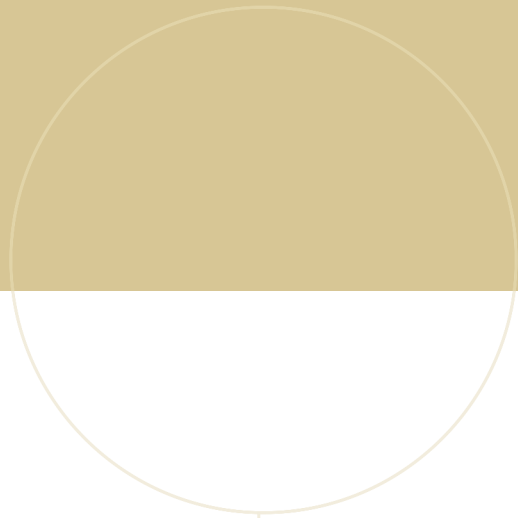
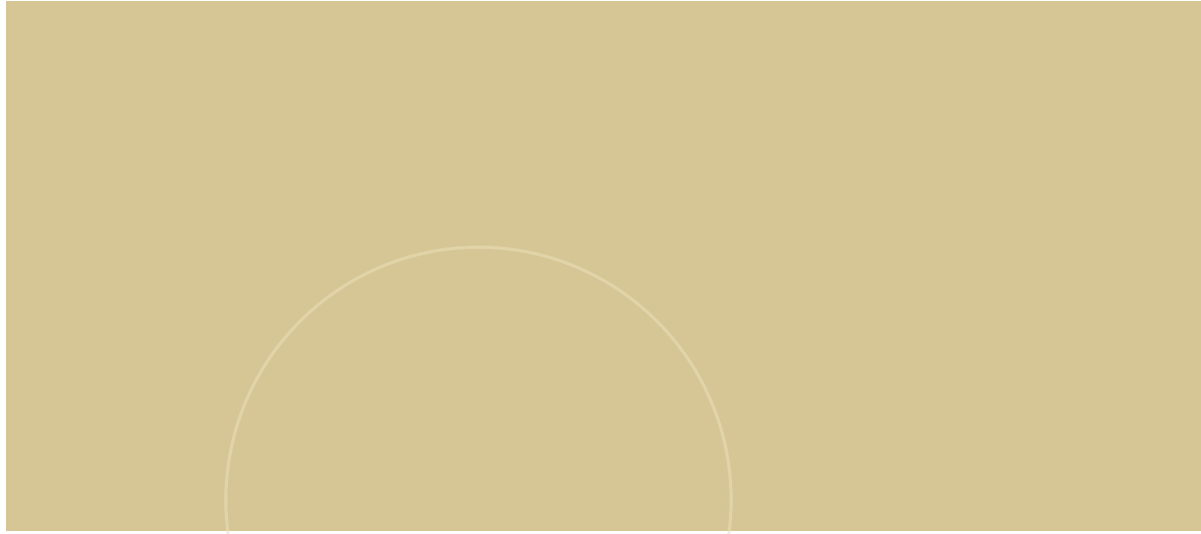
The mechanics are similar to the *M.Xanthus* bacteria, indicating that the model has physical significance.

Future research should be made into simulating AMB+ in a heterogeneous topography.

# Bibliography

- [1] Sriram Ramaswamy. “The Mechanics and Statistics of Active Matter”. In: *Annual Review of Condensed Matter Physics* 1.1 (2010), pp. 323–345. DOI: 10.1146/annurev-conmatphys-070909-104101. URL: <https://doi.org/10.1146/annurev-conmatphys-070909-104101>.
- [2] Karla C. Hernandez Ramos et al. “The environment topography alters the transition from single-cell populations to multicellular structures in *Myxococcus xanthus*”. In: *bioRxiv* (2021). DOI: 10.1101/2021.01.27.428527. eprint: <https://www.biorxiv.org/content/early/2021/01/28/2021.01.27.428527.full.pdf>. URL: <https://www.biorxiv.org/content/early/2021/01/28/2021.01.27.428527>.
- [3] Raphael Wittkowski et al. “Scalar  $\phi^4$  field theory for active-particle phase separation”. In: *Nature Communications* 5.1 (2014). DOI: 10.1038/ncomms5351. URL: <https://doi.org/10.1038/ncomms5351>.
- [4] Elsen Tjhung, Cesare Nardini, and Michael E. Cates. “Cluster Phases and Bubbly Phase Separation in Active Fluids: Reversal of the Ostwald Process”. In: *Phys. Rev. X* 8 (3 2018), p. 031080. DOI: 10.1103/PhysRevX.8.031080. URL: <https://link.aps.org/doi/10.1103/PhysRevX.8.031080>.
- [5] Sriram Ramaswamy. “Active matter”. In: *Journal of Statistical Mechanics: Theory and Experiment* 2017.5 (2017), p. 054002. DOI: 10.1088/1742-5468/aa6bc5. URL: <https://doi.org/10.1088/1742-5468/aa6bc5>.
- [6] Anupam Sengupta. “Microbial Active Matter: A Topological Framework”. In: *Frontiers in Physics* 8 (2020). ISSN: 2296-424X. DOI: 10.3389/fphy.2020.00184. URL: <https://www.frontiersin.org/article/10.3389/fphy.2020.00184>.
- [7] Joakim Stenhammar et al. “Phase behaviour of active Brownian particles: the role of dimensionality”. In: *Soft Matter* 10 (10 2014), pp. 1489–1499. DOI: 10.1039/C3SM52813H. URL: <http://dx.doi.org/10.1039/C3SM52813H>.
- [8] Michael E. Cates and Julien Tailleur. “Motility-Induced Phase Separation”. In: *Annual Review of Condensed Matter Physics* 6.1 (2015), pp. 219–244. DOI: 10.1146/annurev-conmatphys-031214-014710. eprint: <https://doi.org/10.1146/annurev-conmatphys-031214-014710>. URL: <https://doi.org/10.1146/annurev-conmatphys-031214-014710>.
- [9] O. M. Del Cima et al. “Ostwald ripening for air bubbles and decompression illness: phenomenological aspects in diving”. In: (2018). DOI: 10.48550/ARXIV.1806.05673. URL: <https://arxiv.org/abs/1806.05673>.
- [10] Sudipta Pattanayak, Shradha Mishra, and Sanjay Puri. “Ordering kinetics in the active model *B*”. In: *Phys. Rev. E* 104 (1 2021), p. 014606. DOI: 10.1103/PhysRevE.104.014606. URL: <https://link.aps.org/doi/10.1103/PhysRevE.104.014606>.

- [11] Hao Wu. “A review on the Cahn–Hilliard equation: classical results and recent advances in dynamic boundary conditions”. In: *Electronic Research Archive* 30.8 (2022), pp. 2788–2832. ISSN: 2688-1594. DOI: [10.3934/era.2022143](https://doi.org/10.3934/era.2022143). URL: <https://www.aimspress.com/article/doi/10.3934/era.2022143>.
- [12] R. Kenzler et al. “Phase separation in confined geometries: Solving the Cahn–Hilliard equation with generic boundary conditions”. In: *Computer Physics Communications* 133.2 (2001), pp. 139–157. ISSN: 0010-4655. DOI: [https://doi.org/10.1016/S0010-4655\(00\)00159-4](https://doi.org/10.1016/S0010-4655(00)00159-4). URL: <https://www.sciencedirect.com/science/article/pii/S0010465500001594>.
- [13] C. M. Elliott. “The Cahn-Hilliard Model for the Kinetics of Phase Separation”. In: *Mathematical Models for Phase Change Problems*. Ed. by José Francisco Rodrigues. Basel: Birkhäuser Basel, 1989, pp. 35–73. ISBN: 978-3-0348-9148-6. DOI: [10.1007/978-3-0348-9148-6\\_3](https://doi.org/10.1007/978-3-0348-9148-6_3). URL: [https://doi.org/10.1007/978-3-0348-9148-6\\_3](https://doi.org/10.1007/978-3-0348-9148-6_3).
- [14] Marija Milošević. “The Euler–Maruyama approximation of solutions to stochastic differential equations with piecewise constant arguments”. In: *Journal of Computational and Applied Mathematics* 298 (2016), pp. 1–12. ISSN: 0377-0427. DOI: <https://doi.org/10.1016/j.cam.2015.11.019>. URL: <https://www.sciencedirect.com/science/article/pii/S0377042715005646>.
- [15] Elsen Tjhung. *Numerical discretization for active scalar field theory*. URL: <https://elsentjhung.github.io/2020/12/26/discretization.html>. (accessed: 03.02.2023).
- [16] C. M. Pooley and K. Furtado. “Eliminating spurious velocities in the free-energy lattice Boltzmann method”. In: *Phys. Rev. E* 77 (4 2008), p. 046702. DOI: [10.1103/PhysRevE.77.046702](https://doi.org/10.1103/PhysRevE.77.046702). URL: <https://link.aps.org/doi/10.1103/PhysRevE.77.046702>.
- [17] Yibao Li et al. “A conservative numerical method for the Cahn–Hilliard equation with Dirichlet boundary conditions in complex domains”. In: *Computers Mathematics with Applications* 65.1 (2013), pp. 102–115. ISSN: 0898-1221. DOI: <https://doi.org/10.1016/j.camwa.2012.08.018>. URL: <https://www.sciencedirect.com/science/article/pii/S0898122112006463>.
- [18] K. W. Morton and D. F. Mayers. *Numerical Solution of Partial Differential Equations: An Introduction*. 2nd ed. Cambridge University Press, 2005, pp. 75–77. DOI: [10.1017/CB09780511812248](https://doi.org/10.1017/CB09780511812248). URL: [http://math.science.cmu.ac.th/docs/qNA2556/ref\\_na/Morton\\_Numerical%20Solution%20of%20PDE.pdf](http://math.science.cmu.ac.th/docs/qNA2556/ref_na/Morton_Numerical%20Solution%20of%20PDE.pdf).
- [19] Giordano Fausti. “Phase separation in active systems : non-equilibrium fingerprints”. Theses. Université Paris-Saclay, Dec. 2021. URL: <https://theses.hal.science/tel-03750918>.



 **NTNU**

Norwegian University of  
Science and Technology